Single-cell to pre-clinical evaluation of *Trem2*, *Folr2*, and *Slc7a7* as macrophage-associated biomarkers for atherosclerosis

Tiit Örd[1*], Senthil Palani[2*], Judith Giroud Gerbetant[3,4,5], Susanna Bodoy[3,4,5], , Tapio Lönnberg[6,7], Henri Niskanen[1], Aarthi Ravindran[1], Lari Holappa[1], Melody Chemaly[8], Mari Taipale[1], Kadri Õunap[1], Retu Haikonen[1], Husain Talukdar[9], Katyayani Sukhavasi[10], Heidi Liljenbäck[2,11], Jenni Virta[2], Anna-Kaisa Ruotsalainen[1], Clara Pierrot-Blanchet[12], Maxwell W.G. Miner[2], Olli Moisio[2], Noora Rajala[2], Xiang-Guo Li[2,7,13], Philip S. Low[14], Antti Saraste[2,15], Merja Heinäniemi[16], Seppo Ylä-Herttuala[1], Johan LM Björkegren[9], Ulf Hedin[8], Ljubica Matic[8], Laurent Yvan-Charvet[12], Manuel Palacin[4,5], Anne Roivainen[2,7,11≠], Minna U Kaikkonen[1≠]

AFFILIATIONS:
1. A. I. Virtanen Institute for Molecular Sciences, University of Eastern Finland, Kuopio, FI-70211, Finland.
2. Turku PET Centre, University of Turku and Turku University Hospital, Turku, Finland
3. Biosciences Department, University of Vic-Central University of Catalonia (UVic-UCC), Vic, Spain
4. Centro de Investigación Biomédica en Red Enfermedades Raras (CIBERER), Barcelona, Spain
5. Institute for Research in Biomedicine (IRB Barcelona), the Barcelona Institute of Science and Technology (BIST), 08028 Barcelona, Spain.
6. Turku Bioscience Centre, University of Turku and Åbo Akademi University, FI-20520 Turku, Finland
7. InFLAMES Research Flagship, University of Turku, FI-20520 Turku, Finland.
8. Division of Vascular Surgery, Department of Molecular Medicine and Surgery, Karolinska University Hospital and Karolinska Institutet, Stockholm, Sweden
9. Department of Medicine, Karolinska Institutet, Karolinska Universitetssjukhuset, Huddinge, Sweden
10.Department of Cardiac Surgery and The Heart Clinic, Tartu University Hospital and Department of Cardiology, Institute of Clinical Medicine, Tartu University, Tartu, Estonia
11. Turku Center for Disease Modeling, University of Turku, FI-20520 Turku, Finland.
12. Institut National de la Santé et de la Recherche Médicale (Inserm) U1065, Université Côte d'Azur, Centre Méditerranéen de Médecine Moléculaire (C3M), Atip-Avenir, Fédération Hospitalo-Universitaire (FHU) Oncoage, 06204 Nice, France
13. Department of Chemistry, University of Turku, FI-20500 Turku, Finland.
14. Department of Chemistry, Purdue University, West Lafayatte, IN, United States.
15. Heart Center, Turku University Hospital and University of Turku, FI- 20520 Turku, Finland.
16. Institute of Biomedicine, School of Medicine, University of Eastern Finland, Kuopio, Finland.

*Equal 1st authors

≠ Corresponding authors: Anne Roivainen (aroivan@utu.fi) and Minna U Kaikkonen (minna.kaikkonen@uef.fi)

ACCEPTED MANUSCRIPT

Downloaded from https://academic.oup.com/cardiovascres/advance-article/doi/10.1093/cvr/cvaf210/8316259 by Turku University Language Centre user on 10 November 2025

© The Author(s) 2025. Published by Oxford University Press on behalf of the European Society of Cardiology. This is an Open Access article distributed under the terms of the Creative Commons Attribution License (https://creativecommons.org/licenses/by/4.0/), which permits unrestricted reuse, distribution, and reproduction in any medium, provided the original work is properly cited.

ABSTRACT

Aims

Atherosclerosis is a major global health challenge, with limited diagnostic and therapeutic options. Macrophages drive disease progression, but their tissue-specific phenotypes and functions remain poorly defined. This study aims to elucidate macrophage-driven mechanisms by characterizing their functional diversity across key metabolic and vascular tissues.

Methods and Results

We used single-cell RNA sequencing (scRNA-seq) and Translating Ribosome Affinity Purification sequencing (TRAP-seq) to profile macrophage-specific gene programs in a mouse model of atherosclerosis across the aorta, adipose tissue, and liver. Our data highlights tissue-specific macrophage gene programs and identifies markers that are shared across mouse and human plaques. First, we identified soluble *Trem2* as a potential circulating biomarker for differentiating between asymptomatic and symptomatic individuals. Secondly, we leveraged the pronounced expression of *Folr2* and *Slc7a7* to explore the potential of folate and glutamine as PET tracers for disease burden assessment through *in vivo* positron emission tomography (PET) imaging. Finally, we show that knockout of *Slc7a7* inhibits acetylated low-density lipoprotein (AcLDL) uptake and dampens the gene signature linked to lipid-associated macrophages. This suggests that glutamine signaling may play a critical role in foam cell formation, a key event in atherosclerosis.

Conclusions

Our findings provide novel insights into macrophage-specific gene programs during atherosclerosis progression and identify a set of promising biomarkers that can serve as a

ACCEPTED MANUSCRIPT

Downloaded from https://academic.oup.com/cardiovascres/advance-article/doi/10.1093/cvr/cvaf210/8316259 by Turku University Language Centre user on 10 November 2025

resource for future studies. These findings could significantly contribute to improving the diagnosis, monitoring, and treatment of atherosclerosis.

Translational Perspective

In this study, we characterized macrophage-specific biomarkers and their roles in atherosclerosis using advanced imaging and genomic techniques. The identification of soluble TREM2 as a biomarker for differentiating symptomatic from asymptomatic atherosclerosis could significantly enhance early diagnosis and patient stratification in clinical settings. Additionally, exploring Folr2 and Slc7a7 as PET tracers provides a promising avenue for non-invasive assessment of disease burden, potentially allowing for better monitoring of disease progression and treatment efficacy. These findings suggest practical applications in improving personalized treatment plans and could lead to earlier therapeutic interventions, thereby potentially reducing the incidence of severe cardiovascular events.

INTRODUCTION

Atherosclerosis is a complex, chronic inflammatory disease characterized by lipid accumulation in the artery wall leading to plaque formation. A central player in this pathological process is the macrophage, a highly diverse and plastic cell type capable of adopting a spectrum of functional states in response to environmental cues [1]. The concept of diversity of mouse macrophages in healthy tissue has notably been studied by the ImmGen consortium, among others,[2,3] but it has not yet been fully explored in pathological tissues. Given their crucial role in atherosclerosis progression, a better understanding of the gene programs defining the differentiation of macrophage subtypes across various tissues during disease progression is of the utmost importance.

ACCEPTED MANUSCRIPT

Downloaded from https://academic.oup.com/cardiovascres/advance-article/doi/10.1093/cvr/cvaf210/8316259 by Turku University Language Centre user on 10 November 2025

Recent advances in single-cell RNA sequencing (scRNA-seq) have enabled the study of gene expression in specific cell types, including macrophages, with unprecedented resolution and across species[1,4,5]. Much of the current knowledge, however, is derived from studies focusing on a single tissue type, such as the aorta, without observing other peripheral metabolic tissues such as liver and adipose tissue, which are known to affect plaque development through plasma metabolites as well as organ communication[6]. Furthermore, while there has been progress in identifying macrophage-associated genes implicated in atherosclerosis, their translational potential as biomarkers for non-invasive, *in vivo* monitoring of disease burden remains largely unexplored. The development of such biomarkers could revolutionize the diagnosis and management of atherosclerosis. For instance, biomarkers tailored to subclinical diagnosis or for identifying asymptomatic patients may hold significant potential for prevention of myocardial infarction or stroke[7,8]. Simultaneously, the advancement in novel positron emission tomography (PET) radiotracers offers the prospect of a more refined and precise characterization of high-risk plaque[9]. Lastly, the functional role of specific macrophage genes in the progression of atherosclerosis, particularly their contribution to lipid uptake and foam cell formation (a hallmark of atherosclerosis) is poorly understood. A more detailed understanding of these processes could unveil novel therapeutic targets.

In this study, we aim to address these gaps in knowledge. We employed translating ribosome affinity purification sequencing (TRAP-Seq) and scRNA-Seq to profile macrophage-specific gene programs across multiple tissues in a mouse model of atherosclerosis. First, we identified triggering receptor expressed on myeloid cells 2 (*Trem2)* expression in vascular tissue as a marker of plaque burden and as a circulating protein partly capable of distinguishing between asymptomatic and symptomatic plaques. Next, we explored the potential of folate and glutamine as PET tracers, leveraging high expression of folate receptor (*Folr2*) and solute

ACCEPTED MANUSCRIPT

Downloaded from https://academic.oup.com/cardiovascres/advance-article/doi/10.1093/cvr/cvaf210/8316259 by Turku University Language Centre user on 10 November 2025

carrier family 7 member 7 (*Slc7a7),* respectively, in atherosclerosis associated macrophages. Finally, we elucidated the functional role of *Slc7a7* in lipid uptake, establishing its contribution to foam cell formation. Our study offers fresh insights into macrophage gene programs during the development of atherosclerosis and unveils potential biomarkers for monitoring disease burden.

MATERIALS AND METHODS

Atherosclerosis disease stage course mouse experiments

To induce different stages of atherosclerosis, male mice deficient in the low-density lipoprotein receptor and expressing only apolipoprotein B100 ($LDLR^{-/-}ApoB^{100/100}$, strain #003000; Jackson Laboratory, Bar Harbor, ME, USA) were fed with a high-fat diet (HFD; 0.2% total cholesterol, 42% calories from fat, 34% sucrose by weight; TD 88137; Envigo, Madison, WI, USA). For TRAP-Seq, the $LDLR^{-/-}ApoB^{100/100}$ were crossed with mice expressing *Csf1r* promoter 3×FLAG-EGFP-RPL10a transgenic construct[10]. The TRAP-Seq mouse strains used here have been made available in the European Mouse Mutant Archive (EMMA; https://www.infrafrontier.eu/emma/)[11] mouse repository under accession numbers EM:15591 and EM:15575.

The HFD was initiated at different ages to ensure that all groups of mice were matched for age at the end of the study. The mice fed a HFD from 5-6 months of age for 1 month were used as an early disease model, and mice fed a HFD from 3-4 months of age for 3 months were used as an advanced disease model. $LDLR^{-/-}ApoB^{100/100}$ mice fed a chow diet were used as genetic background controls (Prelesion model). Finally, wild type C57Bl/6J mice fed on a

ACCEPTED MANUSCRIPT

Downloaded from https://academic.oup.com/cardiovascres/advance-article/doi/10.1093/cvr/cvaf210/8316259 by Turku University Language Centre user on 10 November 2025

chow diet were used as unaffected controls (Control group). The sample sizes for each experiment are indicated in the figure legends.

All animal experiments were approved by the national Project Authorization Board (permission numbers ESAVI/4567/2018, ESAVI/6772/2018, ESAVI/11751/2021 and ESAVI/17197/2021) and were carried out in compliance with the EU Directive 2010/EU/63 on the protection of animals used for scientific purposes.

TRAP-Seq library generation

Tissue was frozen in liquid nitrogen, pulverized using a Cellcrusher cryo-press (Cellcrusher, Cork, Ireland) and further processed in Lysis buffer with Dounce homogenizer. Lysis buffer was freshly prepared, containing a low-salt/homogenization buffer (20 mM HEPES pH 7.4; Fisher, 10041703), 150 mM KCl (Sigma, 60142), 10 mM MgCl2 (Invitrogen, AM9530G), supplemented with 0.5 mM dithiothreitol (DTT) (Sigma, 10197777001), cOmplete Mini EDTA-free protease inhibitor (Roche 11836170001, one mini tablet/10 mL), 100 µg/mL cycloheximide (Sigma-Aldrich, 1810) in dimethylsulfoxide (DMSO) (Sigma C1988-1G), 0.2 U/µL murine RNase inhibitor (NEB M0314L), and 0.1 U/µL Superasin RNase inhibitor (Thermo Scientific AM2696). The buffer was added to the tissue at 1 mL per 100 mg of tissue, and homogenized samples were centrifuged at 2,000 g for 10 minutes at 4°C to separate debris. Supernatant was collected, mixed with 10% IGEPAL CA630 (Sigma, I8896)] to reach final 1 %v/v and with 1,2-diheptanoyl-sn-glycero-3-phosphocholine (Avanti Polar Lipids, 850306P) in final concentration of 30 mM. Samples were incubated on ice for 5 minutes centrifuged at 20000 g for 10 minutes at 4°C.

Biotinylated Protein L (Pierce #29997) was dissolved in PBS (1 µg/µL) and 120 µL was mixed with 300 µL of Dynabeads MyOne Streptavidin T1 (10 mg/mL; Invitrogen 65602) to form

ACCEPTED MANUSCRIPT

Downloaded from https://academic.oup.com/cardiovascres/advance-article/doi/10.1093/cvr/cvaf210/8316259 by Turku University Language Centre user on 10 November 2025

a bead–protein complex used per sample in pulldown experiments. This complex was employed to capture anti-GFP antibodies, clone 19F7 and clone 19C8, 37.5 µg each, from the Antibody and Bioresource Core Facility at Memorial Sloan Kettering Cancer Center. Beads were incubated with antibodies for 1h in 1mL of low-salt buffer (20 mM HEPES pH 7.4, 10 mM MgCl2, 150 mM KCl, 1 % IGEPAL CA630, 0.5 mM DTT and 100 µg/mL cycloheximide) and washed 4 times before use. To extract bulk RNA (input RNA), 5% of cell lysate was set aside and mixed with lysis buffer from the RNeasy Kit (Qiagen, 74104). The remaining lysate was incubated with pre-prepared antibody-Dynabead affinity matrix for 1-2 hours at 4°C. To enhance RNA purity, the beads were then washed three times with 1 mL high-salt buffer (20 mM HEPES pH 7.4, 350 mM KCl, 5 mM MgCl2, 1% IGEPAL CA630, 1 mM DTT, and 100 µg/mL cycloheximide). RNA was extracted using the Absolutely RNA Nanoprep Kit (#400753, Agilent Technologies, Santa Clara, California), producing the immunoprecipitated (IP) RNA sample.

RNA quality and concentration were assessed using the Bioanalyzer RNA 6000 Pico assay (Agilent). Library preparation was conducted using the SMARTer Stranded Total RNA-Seq Kit v2 (TaKaRa Bio, 634411, 634412), followed by single-end sequencing on the Illumina NextSeq 500 platform.

Single cell RNA-Seq data sources and processing

scRNA-Seq from mouse aorta and epididymal white adipose tissue was obtained from the same disease stages (genotype and diet conditions) as the TRAP-Seq and PET imaging experimental groups. The generation of the aorta scRNA-Seq data (GEO accession GSE205930) is described in detail in [12], while the adipose data (GEO accession GSE241552) is described in [13]. Briefly, mice were sacrificed, perfused with cold PBS-heparin, and dissected on ice. The extracted tissues were minced with a scalpel and enzymatically dissociated to a

ACCEPTED MANUSCRIPT

Downloaded from https://academic.oup.com/cardiovascres/advance-article/doi/10.1093/cvr/cvaf210/8316259 by Turku University Language Centre user on 10 November 2025

single-cell suspension, followed by red blood cell lysis and magnetic dead cell removal. The Chromium Single Cell 3' Kit (v2 Chemistry; 10x Genomics) was used for scRNA-Seq library preparation.

For mouse scRNA-Seq, data from both tissues was processed as described in our previous work [12]. Briefly, the 10x Genomics Cell Ranger count pipeline (version 3.0.2) with the mm10 reference package (version 3.0.0) was used for cell calling and gene quantification. Briefly, the Seurat[14] (version 3.1.0) R package was used to first run the standard (log normalization-based) RNA processing workflow recommended by the package authors on each sample individually. DecontX[15] (from the celda R package version 1.1.6) was used with default parameters remove ambient RNA contamination. Cells with high (>0.3) estimated contamination fraction, potentially doublets, were excluded prior to marker finding. Immune cell clusters were identified by expression of *Ptprc* (encoding CD45) and retained. Finally, immune cells across aorta and adipose libraries were integrated using the Seurat CCA method[14]. The integrated cells were clustered using Seurat FindClusters with resolution 0.8 (default) and the resulting clusters were manually renamed after observing the top marker genes. Cell cycle phase scores were calculated using the Seurat CellCycleScoring function with the built-in gene lists for the S and G2/M phases.

To calculate marker genes in scRNA-Seq, the Seurat FindMarkers command was used to perform a Wilcoxon Rank Sum test. P-value < 0.05 after adjustment for multiple testing by FDR was considered significant. The cutoffs used for minimum fraction of cells expressing the gene and for minimum fold change are stated in the Table headers.

Mouse liver macrophage/monocyte scRNA-Seq data from a previously published diet time course study[16] was obtained from https://www.livercellatlas.org (access date: January 7, 2025). We used the original authors' count matrix and cell annotations which were already subsetted

ACCEPTED MANUSCRIPT

Downloaded from https://academic.oup.com/cardiovascres/advance-article/doi/10.1093/cvr/cvaf210/8316259 by Turku University Language Centre user on 10 November 2025

to include only macrophages/monocytes. We retained all the original experimental conditions (standard and Western diet, and 12-, 24- and 36-week time-points). The count matrix was processed using the default Seurat log-normalization RNA workflow (as for aorta and adipose tissue), and the 3-tissue (adipose–aorta–liver) integration of macrophage/monocyte cells was done using CCA (as for aorta–adipose integration, referenced above).

Human coronary artery scRNA-Seq was obtained from GEO (accession GSE131778) as count matrices generated by the original authors[17]. The counts were processed using the RNA workflow suggested by the authors of Seurat version 3.1.0[14] and cell types were annotated based on the gene lists provided in the original publication.

The protein annotations (membrane-localized, receptor, and metabolic proteins) were based on the Human Protein Atlas[18] (release 22).

Biobank of Karolinska Endarterectomy (BiKE)

Patients undergoing surgery for symptomatic (S) or asymptomatic (AS), high-grade (>50% NASCET)[19] carotid stenosis at the Department of Vascular Surgery, Karolinska University Hospital and Department of Surgery, Vascular section, Södersjukhuset, Stockholm, Sweden, were enrolled in the study and clinical data recorded on admission. Symptoms of plaque instability were defined as transitory ischemic attack (TIA), minor stroke (MS) and amaurosis fugax (AF). Patients without qualifying symptoms within 6 months prior to surgery were categorized as AS and indication for carotid endarterectomy (CEA) was based on results from the Asymptomatic Carotid Surgery Trial (ACST)[20]. Carotid plaques and blood samples were collected at surgery and retained within the Biobank of Karolinska Endarterectomies (BiKE). The BiKE study cohort demographics, details of sample collection, processing and large-scale analyses were as previously described[21-23].

ACCEPTED MANUSCRIPT

Downloaded from https://academic.oup.com/cardiovascres/advance-article/doi/10.1093/cvr/cvaf210/8316259 by Turku University Language Centre user on 10 November 2025

For microarrays, n = 127 plaques were divided transversally at the most stenotic part and the proximal half of the lesion used for RNA preparation. Normal artery controls were obtained from nine macroscopically disease-free iliac arteries and one aorta from organ donors without a history of cardiovascular disease (n = 10).

The following five Olink® panels were used in BiKE plasma profiling: Olink® Target 96 Cardiometabolic, Olink® Target 96 CVD II, Olink® Target 96 CVD III, Olink® Target 96 Development, and Olink® Target 96 Immuno-Oncology. The Olink® platform uses proprietary Proximity Extension Assay (PEA) technology and a readout based on Next Generation Sequencing (NGS) in Illumina NovaSeq 6000. OlinkAnalyze package was used to perform the standard quality control (QC) on this panel of protein analytes using the NPX function and relevant QC parameters as suggested by the package vignette to remove the outlier samples that do not meet their standard quality flags. . A total of 100 plasma samples from BiKE patients (50 asymptomatic and 50 symptomatic) were analysed. In brief, two specific antibodies bind the target protein, bringing two single stranded DNA tags into close proximity. Then, the double stranded tag was cleaved and amplified by PCR and further indexed to allow the preparation of libraries, which were then sequenced using Illumina's NovaSeq platform. Relative expression values (normalized protein expression, NPX) were on a log2 scale and are derived from the qPCR step Ct values. One NPX difference corresponds to 2-fold in protein concentration.

All human samples in BiKE were collected with informed consent from patients or organ donors' guardians. Human studies were approved by the regional Ethical Committee and followed the guidelines of the Declaration of Helsinki. The full microarray data (GSE21545) has been deposited at NCBI Gene Expression Omnibus and is publicly available. The individual human data cannot be deposited or shared because of the GDPR and ethics laws that regulate the privacy of individuals that participated in the study.

ACCEPTED MANUSCRIPT

Downloaded from https://academic.oup.com/cardiovascres/advance-article/doi/10.1093/cvr/cvaf210/8316259 by Turku University Language Centre user on 10 November 2025

Data analysis of the selected genes of interest was done using GraphPad Prism v.10 using a two-sided Student's t-test assuming non-equal deviation. Correlation analyses were performed using the Pearson method. Results are displayed as mean ± SD and threshold for significance is $P<0.05$.

Stockholm-Tartu Atherosclerosis Reverse Networks Engineering Task (STARNET)

The STARNET study cohort demographics, details of sample collection, processing and large-scale analyses have been previously described.[24,25] Patients diagnosed with coronary artery disease (CAD) were enrolled at the Department of Cardiac Surgery, Tartu University Hospital. Informed consent was obtained from all subjects (Ethics Review Committee on Human Research of the University of Tartu, IRB no:289/T-12). Each enrolled participant completed a questionnaire to assess disease history, current drug regimens, and lifestyle (e.g., daily activity, alcohol consumption, and smoking). Inclusion criteria for individuals with CAD, were eligible for coronary artery bypass surgery (CABG) and, for controls, eligible for open-heart surgery for reasons other than CABG (primarily valve replacement following aortic stenosis) and a pre-operative angiogram ruling out obstructive CAD. For both individuals with CAD and controls, the absence of other severe systemic disease such as active cancer or inflammatory disease was also required. During open-breast surgery, atherosclerotic aortic arterial wall (AOR), mammary artery (MAM), only in individuals with CAD), visceral abdominal fat (VAF), subcutaneous fat (SF), liver (LIV) and skeletal muscle (SKLM) biopsies were obtained and immediately kept in Allprotect Tissue Reagent (Qiagen) and frozen at −80 °C. Preoperative blood samples were collected for biochemical screens, plasma, whole blood RNA and DNA isolations. EDTA blood tubes were centrifuged for 10 min (RT) 300 rcf (acceleration 4,

ACCEPTED MANUSCRIPT

Downloaded from https://academic.oup.com/cardiovascres/advance-article/doi/10.1093/cvr/cvaf210/8316259 by Turku University Language Centre user on 10 November 2025

deceleration 0). The plasma (supernatant) was collected in 2 ml eppendorf tubes and frozen at -80 C.

Tissue protein isolation was done using a 10x RIPA buffer (Sigma, R0278) with protease inhibitor cocktail (cOmplete™, Mini Protease Inhibitor Cocktail, Roche). Weigh tissue (much needed for proper addition of buffer so that protein does not get diluted). Add buffer with inhibitor in the ratio of 1:4 (i.e to 0.1 g of tissue add 0.4ml of buffer with inhibitor). All steps must be carried out at 2-8C. Homogenize on ice using ultra-turrax homogeniser till the tissue is properly minced. Incubate/vortex on ice on shaker for 1hr. Centrifuge at 5000rpm for 15mins at 4C. Store supernatant and discard the pellet. Measure tissue protein isolated (supernatant) using Bradford reagent (TheromFisher) in microplate reader.

Proteomic profiling was conducted using the Olink Explore 3072 platform, a high-throughput proximity extension assay (PEA)-based technology[26]. Biological samples were collected and processed under standardized conditions before incubation with oligonucleotide-labeled antibody pairs. Following proximity extension, pre-amplification, and next-generation sequencing (NGS) on an Illumina NovaSeq 6000 system, raw sequencing data were processed using Olink's proprietary software. Normalized Protein eXpression (NPX) values were calculated using the Olink normalization algorithm to account for inter-sample variation. To assess the associations of TREM2 between plasma and tissue (AOR, LIV, MAM, SKLM) protein expression and clinical variables Pearson correlation analysis was used.

PET chemicals and reagents

$^{68}GaCl_3$ was obtained from a $^{68}Ge/^{68}Ga$ IGG-100 generator (Eckert & Ziegler, Valencia, CA, USA) via elution with 0.1 M hydrochloric acid in water. The NOTA-folate precursor was provided

ACCEPTED MANUSCRIPT

Downloaded from https://academic.oup.com/cardiovascres/advance-article/doi/10.1093/cvr/cvaf210/8316259 by Turku University Language Centre user on 10 November 2025

by Professor Phillip Low from Purdue University, Department of Chemistry (West Lafayatte, IN, USA). The tosylated precursor for (2S,4*R*)-4-[^{18}F]fluoroglutamine (^{18}F-FGln) synthesis and the non-radioactive reference compound FGln were provided by the Organic Synthesis Core Facility at Memorial Sloan Kettering Cancer Center, New York, NY, USA. The cassettes for 2-deoxy-2-[^{18}F]fluoro-*D*-glucose (^{18}F-FDG) synthesis were purchased from GE Healthcare (Waukesha, WI, USA). Other chemicals and reagents were purchased from commercial vendors.

PET tracer radiosynthesis

The chemical structures and preparation of gallium-68-labeled 1,4,7-triazacyclononane-1,4,7-triacetic acid (NOTA)-conjugated folate (^{68}Ga-FOL) and ^{18}F-FGln have previously been reported[27-29]. The preparation of ^{18}F-FDG was accomplished using a fully automated cassette-based system and a FASTLab® radiosynthesis device[30], following Good Manufacturing Practices. Prior to the release of all synthesized batches, quality control was conducted through high-performance liquid chromatography (HPLC) for all compounds with additional thin-layer chromatography also being used for ^{18}F-FDG. ^{68}Ga-FOL, ^{18}F-FGln and ^{18}F-FDG have been validated for studying atherosclerosis in our previous studies[27,28].

PET/CT imaging

The mice were fasted for 3–4 hours prior to imaging, anesthetized with isoflurane (4–5% induction, 1.5–2.5% maintenance), intravenously cannulated, and placed on a heating pad in the PET/CT scanner (Inveon Multimodality; Siemens Medical Solutions, Knoxville, TN, USA). The mice received ^{18}F-FDG (13.9 ± 0.7 MBq), ^{18}F-FGln (14.2 ± 0.8 MBq) or ^{68}Ga-FOL (20.1 ±

ACCEPTED MANUSCRIPT

Downloaded from https://academic.oup.com/cardiovascres/advance-article/doi/10.1093/cvr/cvaf210/8316259 by Turku University Language Centre user on 10 November 2025

1.3 MBq) intravenously via the tail vein cannula (Table 13) for a 60 minute dynamic PET acquisition. An iodinated contrast agent (100 µL eXIATM160XL; Binitio Biomedical, Ottawa, ON, Canada) was intravenously injected after PET imaging, and a 10 minute high-resolution CT was performed for anatomical reference. The list-mode acquired PET data was reconstructed with an iterative three-dimensional ordered subset expectation maximization using maximum a priori with shifted Poisson distribution (OSEM3D/SP-MAP) algorithm into 10 × 30 s, 5 × 60 s, 10 × 300 s time frames. CT images were reconstructed with Feldkamp algorithm.

PET/CT images were analyzed using Carimas 2.10 software (Turku PET Centre, Turku, Finland; www.turkupetcentre.fi/carimas/). Contrast-enhanced CT was used as an anatomical reference to define the regions of interest (ROI) in the aortic arch, vena cava (representing blood), and myocardium, as previously described[31]. The results of the PET/CT analysis were expressed as standardized uptake values (SUVs), taking into account the injected radioactivity dose (minus remaining dose in the cannula and tail) and animal's body weight. To accurately quantify aortic arch uptake, the radioactivity concentration in the blood was taken into account, and the maximum target-to-background ratio (TBR) was calculated by the formula: $SUV_{max,\ aortic\ arch}/SUV_{mean,\ blood}$, at 40–60 minutes post-injection.

Ex Vivo biodistribution analysis

To study the biodistribution of tracers in different tissues, mice were placed under deep isoflurane anesthesia (4–5% induction, 1.5–2.5% maintenance). At 70 minutes post-injection, blood samples were obtained through cardiac puncture. After euthanizing the mice by cervical dislocation, the tissues were dissected and weighed. Radioactivity was measured using a γ-

ACCEPTED MANUSCRIPT

Downloaded from https://academic.oup.com/cardiovascres/advance-article/doi/10.1093/cvr/cvaf210/8316259 by Turku University Language Centre user on 10 November 2025

counter (Triathler 3″; Hidex, Turku, Finland). The results were expressed as SUVs calculated as radioactivity concentration (becquerels per gram of tissue) normalized for injected radioactivity dose (compensated for the remaining radioactivity in the tail and cannula) and animal body weight.

Autoradiography, histology, and immunostaining

Following *in vivo* PET/CT imaging and *ex vivo* gamma counting, tracer uptake in the aorta was studied in more detail using *ex vivo* digital autoradiography. The aorta was embedded in optimal cutting temperature (OCT) compound, frozen on dry ice-cooled isopentane, and cut into 20 µm and 8 µm cryosections. The 20 µm cryosections were used for analysis of tracer distribution by quantitative digital autoradiography, as previously described[31]. The sections were exposed to a Fuji Imaging Plate BAS-TR2025 (Fuji, Tokyo, Japan) for at least 4 hours for ^{18}F-FDG and ^{18}F-FGln, and 3 hours for ^{68}Ga-FOL, and then scanned by a Fuji Analyzer BAS-5000. The sections were stored at −70°C after scanning, until they were stained with hematoxylin–eosin (H&E). Stained slides were scanned with a digital slide scanner (Pannoramic 250 Flash; 3DHISTECH, Ltd., Budapest, Hungary).

The analysis of autoradiographs was performed using Tina 2.1 software (Ravtest Isotopenmessgeräte, GmbH, Straubenhardt, Germany). The results were expressed as photostimulated luminescence per square millimeter (PSL/mm^2) normalized with the injected radioactivity dose and body mass, and corrected for decay of radioactivity.

Consecutive adjacent 8 µm aortic sections were used to investigate co-localization of ^{18}F-FGln and ^{68}Ga-FOL in Mac-3-positive macrophages, glutamine transporter Slc7a7-positive macrophages and Folr2-positive macrophages. The sections were incubated with either anti-mouse Mac-3 antibody (working dilution 1:1,000; catalog number: 550292; BD Biosciences,

ACCEPTED MANUSCRIPT

Downloaded from https://academic.oup.com/cardiovascres/advance-article/doi/10.1093/cvr/cvaf210/8316259 by Turku University Language Centre user on 10 November 2025

Franklin Lakes, NJ, USA), anti-SLC7A7 antibody (working dilution 1:1,000; catalog number: PA5-113527; Thermo Fisher Scientific, Waltham, MA, USA), or anti-FR-β antibody (working dilution 1:150; Biorbyt, Cambridge, UK). Then, corresponding secondary antibodies were added, and a color reaction was developed using 3.3′-diaminobenzidine (Bright-DAB, BS04-110; ImmunoLogic, Duiven, the Netherlands). Finally, slides were counterstained with hematoxylin and mounted.

Mouse hearts and livers were collected, formalin-fixed, and embedded in paraffin for histological characterization of atherosclerotic lesions at the level of the aortic root and hepatic steatosis and steatohepatitis[28,31]. Aortic sections of 6 µm thickness were cut transversely at the level of the coronary ostia, and consecutive sections were stained with H&E, modified Movat's pentachrome[31,32] and anti-Mac-3 (1:100; product: as above), anti-iNOS (1:100, catalog number: ab15323; Abcam, Cambridge, United Kingdom), anti-MRC-1 (1:2000, catalog number: ab64693; Abcam, Cambridge, United Kingdom), anti-SLC7A7 (1:1500; product: as above), anti-FR-β (1:150; product: as above), and anti-TREM2 (1:2000, catalog number: PA5-87933; Thermo Fisher Scientific Waltham, MA, USA) antibodies followed by subsequent second-stage antibodies and color reaction developed using DAB. Liver sections were stained with H&E. The stained slides were scanned with a slide scanner (Pannoramic Flash) and the images captured using a CaseViewer 2.4 software (3DHISTECH Ltd., Budapest, Hungary).

Quantification of soluble TREM2 (sTREM2) protein from mouse plasma

Mouse blood was collected into an EDTA Microtainer collection tube (BD Medical) and centrifuged to obtain plasma. For mouse sTREM2 ELISA assay, a 96-well plate was coated with anti-TREM2 antibody (MAB17291-100, 1:1000, R&D Systems) in coating buffer (50 mM bicarbonate buffer, pH 9.6) and incubated overnight at 4°C. After incubation, the plate was

ACCEPTED MANUSCRIPT

Downloaded from https://academic.oup.com/cardiovascres/advance-article/doi/10.1093/cvr/cvaf210/8316259 by Turku University Language Centre user on 10 November 2025

washed three times with washing buffer (0.05% Tween-20 in PBS). Next, the plate was blocked with blocking buffer (1% Bio-Rad Block Ace in PBS) for 4 hours at room temperature (RT), washed with PBS, and then incubated with 15 µL of plasma samples and 85 µL of assay buffer (1% BSA and 0.05% Tween-20 in PBS) overnight at 4°C. Recombinant mouse TREM2 (50149-M08H, Sino Biological) was employed to create standard curves. The plates were washed five times with washing buffer, followed by a 1-hour incubation at RT with a biotinylated mouse anti-TREM2 antibody (BAF1729, 1:3000, R&D Systems). After three more washing steps, the plates were treated with Streptavidin Poly-HRP40 Conjugate (65R-S104PHRP, 1:3000, Fitzgerald) for 1 hour in the dark. After five additional washes with washing buffer, the plates were developed by adding the TMB substrate (3,3',5,5'-Tetramethylbenzidine Liquid Substrate, Super Slow, T5569, Sigma-Aldrich). The reaction was terminated by adding stop solution (1M H_3PO_4) and the samples were read at 450 nm using a CLARIOstar microplate reader (BMG Labtech).

Primary bone marrow-derived macrophages from *Slc7a7* knockout mouse model

Slc7a7-LysM mice[33,34] were generated in C57Bl/6J genetic background and all experiments were conducted under the approved project (DARP nº9177) by Use Committee from Parc Científic from Barcelona.

Bone marrow (BM) cells were obtained from 12-week-old mice. Mice were euthanized by placing them in a CO_2 chamber for approximately 20 seconds followed by cervical dislocation. No anesthesia was administered to the mice. After sacrificing, the femurs and tibiae were extracted, and BM cells were flushed out. The cell suspension was lysed for 5 min in erythrolysis buffer (R&D Systems, Minnesota, USA) at room temperature and then washed, resuspended, and cultured in 3 different 15-cm diameter plates, for 7 days, with Dulbecco's Modified Eagle Medium (DMEM) supplemented with 10% heat-inactivated fetal bovine serum (FBS), 50 U/mL

ACCEPTED MANUSCRIPT

Downloaded from https://academic.oup.com/cardiovascres/advance-article/doi/10.1093/cvr/cvaf210/8316259 by Turku University Language Centre user on 10 November 2025

penicillin, 50 µg/mL streptomycin and 50 ng/mL of recombinant macrophage colony-stimulating factor (M-CSF) (Peprotech, Massachusetts, USA) or 30% of L-Cell conditioned medium. Six days after seeding, cells were harvested and re-seeded with the previously mentioned conditioned medium for 24 h. For foamy macrophage experiments 30,000 cells were seeded, and macrophages were treated for 24 h with either 100 µg/mL oxidized-LDL, 50 µg/mL acetylated-LDL or vehicle (phosphate-buffered saline, PBS). Cells were then washed and stained with Oil Red O staining to measure lipid droplets inside macrophages. For RNA-Seq analysis, 100,000 cells were seeded and treated with either 100 µg/mL oxidized-LDL, 50 µg/mL acetylated-LDL or vehicle (PBS) for 24 h. Total RNA was isolated using the Qiagen RNeasy Micro Plus kit with the QIAshredder option for lysate homogenization and the gDNA eliminator column for removal of genomic DNA. RNA-Seq libraries were prepared using the SMARTer Stranded Total RNA-Seq Kit v2 (TaKaRa Bio) according to the manufacturer's recommendations and the libraries were single-end sequenced on an Illumina NextSeq 500 instrument.

Bone marrow transplantation and [^{14}C]glutamine uptake

Animal protocols were approved by the Institutional Animal Care and Use Committee of the French Ministry of Higher Education and Research and the Mediterranean Center of Molecular Medicine (Inserm U1065) and were undertaken in accordance with the European Guidelines for Care and Use of Experimental Animals.

Female *Ldlr*$^{-/-}$ recipient mice were irradiated 16 hours prior to bone marrow transplantation and then received an *i.v.* injection of 4 x 10^6 bone marrow cells extracted from *Slc7a7*-LysM knockout[34] donor mice. The mice were allowed to recover for five weeks before being placed on an atherogenic diet (Western diet, TD88137, Ssniff) for 11 weeks. ^{14}C-labeled glutamine

ACCEPTED MANUSCRIPT

Downloaded from https://academic.oup.com/cardiovascres/advance-article/doi/10.1093/cvr/cvaf210/8316259 by Turku University Language Centre user on 10 November 2025

uptake was assessed as described previously[35]. A total of 2 μCi of ^{14}C-labeled glutamine was *i.v.* injected, and the mice were euthanized 15 min later. Aortas were collected, and the surrounding adipose tissue was carefully dissected and removed. The aortic tissues were homogenized in a 5% $HClO_4$ solution, and the radioactivity in the extract was measured and expressed as total radioactivity per sample.

RNA-Seq and TRAP-Seq data processing

For both RNA-Seq and TRAP-Seq, sequencing reads were processed using the nf-core[36] RNA-Seq pipeline to carry out adapter and quality trimming using Trim Galore (https://doi.org/10.5281/zenodo.7598955) followed by alignment to the mm10 mouse genome with STAR[37] and gene quantification using the Ensembl release 93 mouse transcriptome[38]. Lowly expressed genes were filtered out using the edgeR[39] (version 3.24.3) function filterByExpr, requiring at least 15 counts per group and 5 counts in at least one sample in the case of TRAP-Seq. For BMDM RNA-Seq, the requirements were 10 and 2 counts, respectively, on account of their lower sequencing depth. DESeq2[40] (version 1.22.2) was used for differential expression testing and $P < 0.05$ after adjustment for multiple testing by FDR was considered significant. To define macrophage-enriched genes in TRAP-Seq, DESeq2 was used to compare the counts from the macrophage-enriched RNA samples (IP fraction) to the unenriched RNA samples (INPUT fraction) from the same tissue samples. Genes with FDR < 0.05 and log2 fold change > 1 were considered macrophage-enriched. The fgsea R package[41] (version 1.25.1) was used to perform gene set enrichment analysis. Reactome pathways were obtained from MSigDB (mouse release 2024.1)[42]. All pathways with 10-1000 genes were considered. To filter significantly enriched pathways into a set of non-redundant pathways, the collapsePathways function from the fgsea package was run with default parameters.

ACCEPTED MANUSCRIPT

Downloaded from https://academic.oup.com/cardiovascres/advance-article/doi/10.1093/cvr/cvaf210/8316259 by Turku University Language Centre user on 10 November 2025

Statistical Analysis

Results are presented as the mean ± standard deviation (SD). A two-tailed unpaired Student's *t* test in Microsoft Excel was used to analyze differences between the groups. *P*-values <0.05 were considered statistically significant.

Data availability

The raw sequencing data has been deposited in NCBI GEO under accessions GSE254395 (reviewer token alsraieejvizhax), GSE254396 (reviewer token ipqxskykrdclpsx), and GSE205929 (TRAP-Seq), and GSE254398 (BMDM RNA-Seq; reviewer token qradsumodnsvrqf). BiKE transcriptomic dataset is available from NCBI GEO with accession number GSE21545.

RESULTS

Identification of cross-tissue macrophage markers for disease monitoring using TRAP-Seq

Cross-tissue atlases provide insights into the tissue-specific and tissue-agnostic attributes of cell types playing roles in disease. Here, we sought to investigate the macrophage specific gene expression profiles across atherosclerosis-relevant tissues using the LDLR$^{-/-}$ApoB$^{100/100}$ mouse model subjected to 0 (prelesion), 1 (early disease), and 3 (advanced disease) months of high fat diet (HFD), alongside C57Bl/6J control mice (Figure 1A). Upon examination of aortic root sections using histology, we observed atherosclerotic lesions with increasing intima-to-

ACCEPTED MANUSCRIPT

Downloaded from https://academic.oup.com/cardiovascres/advance-article/doi/10.1093/cvr/cvaf210/8316259 by Turku University Language Centre user on 10 November 2025

media ratio as the disease progressed (Supplementary Figure 1A-B). In the advanced stage, lesions exhibited a prominent necrotic core and a fibrous cap (Supplementary Figure 1A). As a result of HFD feeding, body weight increased by 27.6% and 32.1%, for 1- and 3-month HFD, respectively, compared to chow diet-fed mice (Supplementary Figure 1C). In the liver, micro- and macrovesicular steatosis was evident after 1 or 3 months of HFD, along with mild infiltration and activation of immune cells, but the protocols did not induce steatohepatitis (Supplementary Figure 1D).

First, we utilized the TRAP-Seq technique to characterize the macrophage-specific translatome within the aorta, liver, and adipose tissue of the mice. TRAP-Seq is a cost-effective technique that allows the selective isolation of translated mRNAs from specific cell types, in this case, macrophages, by driving the expression of EGFP-RPL10a fusion gene under the *Csf1r* promoter[10] (Supplementary Figure 2A-B). The macrophage specific tagging was confirmed by histological analysis of the EGFP-RPL10a transgene expression (Supplementary Figure 2C-D), as well as the enrichment of macrophage markers *Csfr1*, *Lyz2* (encodes LysM), *Adgre1* (F4/80), *Lamp2* (Mac-3), *Nos2* (iNOS) and *Mrc1*, and the depletion of tissue specific markers *Apoa1* (liver; hepatocyte), *Myl9* (aorta; smooth muscle cell) and *Lep* (adipose tissue; adipocyte) (Supplementary Figure 3). To assess the tissue-specific and temporal enrichment of macrophage-specific genes, we analyzed the differences between the immunoprecipitated (IP) RNAs and the input RNA. This analysis identified a substantial number of macrophage-enriched genes (defined as FDR < 0.05 and $\log_2$ fold change > 1), including 2071genes in the aorta, 2040 genes in adipose tissue, and 4194genes in the liver (Figure 1B-C, Supplementary Tables 1-3). The increased number of results in liver appears to be a consequence of larger effect sizes (IP vs Input ratios) as well as lower variability between replicates, particularly for IP samples (Supplementary Figure 4A-B). Total sequencing depth and the number of genes

ACCEPTED MANUSCRIPT

Downloaded from https://academic.oup.com/cardiovascres/advance-article/doi/10.1093/cvr/cvaf210/8316259 by Turku University Language Centre user on 10 November 2025

detected were similar for all tissues (Supplementary Figure 4C-D). The bulk tissue (Input) expression levels of *Csf1r* were also similar (Supplementary Figure 3). Since the lower variability was especially evident among liver IP samples (Supplementary Figure 4B), it is possible that the overall high RNA content of liver (per mg of tissue) led to a more efficient TRAP process.

Overall, the contributions of tissue and disease appeared to be of the same order of magnitude for each tissue, with a couple hundred genes being associated mostly with tissue or mostly with disease stage. A large fraction of disease stage associated genes identified through TRAP-Seq were shared across the three tissues as exemplified by *Csf1r*, *Mrc1* and *Fcgr3* (Figure 1C-D, Supplementary Tables 1-3). Still, several disease stage specific genes were identified including significant enrichment of *Spp1* and *Mfge8* in the aorta from prelesion stage onwards and a gradual increase of *Igf2r* in adipose tissue and *Plec* in liver during disease progression.

We also saw that hundreds of genes consistently showed enrichment across tissues supporting the similarity of macrophage gene expression programs and the possibility to identify changes which are associated with systemic inflammatory effects of atherosclerotic conditions (Figure 1E, Supplementary Tables 1-3). The top genes include *Mmp9*, *Clec4a3*, *Fcgr1* and members of the *C1q* family (*C1qa-c*). Again, also tissue specific genes were identified, as demonstrated by liver specific expression of *Adamdec1*, *Dleu7*, and *Crip1*, markers of Kupffer cells, and aorta specific expression of *Ctsl* and *Spp1*.

Pathway enrichment analysis (Supplementary Table 4) revealed that general immune and macrophage gene sets were the most strongly overrepresented across all three TRAP-Seq tissues, consistent with macrophage expression profiles. Comparative enrichment analysis between tissues also highlighted distinct features, including lipoprotein and heme processing

ACCEPTED MANUSCRIPT

Downloaded from https://academic.oup.com/cardiovascres/advance-article/doi/10.1093/cvr/cvaf210/8316259 by Turku University Language Centre user on 10 November 2025

in the aorta and extracellular matrix-related functions in adipose tissue (Figure 1F). Taken together, these findings suggest that while there is a core set of macrophage genes across different tissues, there are also unique sets of genes that are specifically regulated in a tissue-dependent manner. This supports the evidence that macrophages adapt their gene expression in response to the local environment but also demonstrates disease stage-specific differences. Identifying these genes could provide a valuable resource for further investigation.

ACCEPTED MANUSCRIPT

Downloaded from https://academic.oup.com/cardiovascres/advance-article/doi/10.1093/cvr/cvaf210/8316259 by Turku University Language Centre user on 10 November 2025

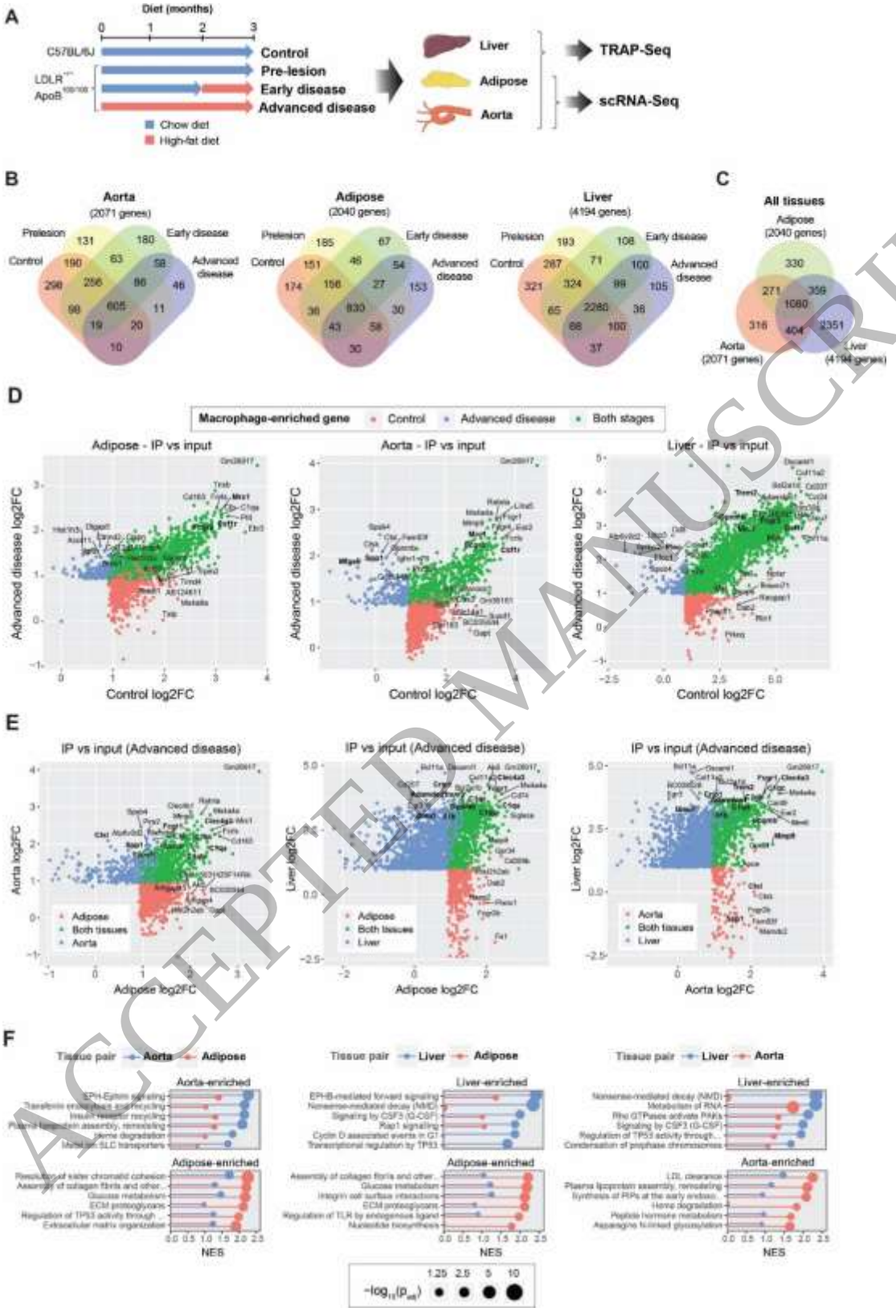

Figure 1. Identification of macrophage specific gene expression using TRAP-Seq. (**A**) Schematic overview of the experimental setup. (**B**) Venn diagrams comparing the number of

ACCEPTED MANUSCRIPT

Downloaded from https://academic.oup.com/cardiovascres/advance-article/doi/10.1093/cvr/cvaf210/8316259 by Turku University Language Centre user on 10 November 2025

genes displaying macrophage-enriched expression in TRAP-Seq of aorta, adipose tissue, and liver, comparing between control, prelesion, early and advanced disease stages. Macrophage-enriched expression was defined as FDR < 0.05 and log2 fold change (log2FC) > 1 between the TRAP-Seq immunoprecipitated RNA and the input RNA. (**C**) Venn diagram compiling the macrophage-enriched genes in adipose, aorta and liver tissues across all disease stages, illustrating the common and unique macrophage-specific gene expression. Macrophage-enriched expression was defined as in panel B. (**D**) Scatter plots comparing the gene expression changes between control (chow diet) and advanced disease stage (3 months high-fat diet) in adipose tissue (left), aorta (middle), and liver (right). (**E**) Scatter plots comparing the macrophage-enriched gene expression between adipose tissue, aorta, and liver of $LDLR^{-/-}ApoB^{100/100}$ mice fed a high-fat diet for 3 months (indicative of advanced disease stage). For panels D and E, each scatter plot shows the log2 FC of TRAP IP vs input RNA, comparing between either two disease stages (D) or tissues (E). Blue and red dots indicate genes classified as markers in one comparison, and green indicates marker in both conditions. **(F)** Gene set enrichment analysis of Reactome pathways in TRAP-Seq data from three tissues. In each tissue, significantly enriched pathways were selected and filtered to remove redundant pathways. Comparing two tissues, the pathways with the largest differences in enrichment (NES, normalized enrichment score) were plotted. P_{adj}, enrichment p-value adjusted by FDR. For panels B–F (TRAP-Seq), 6 mice per group were analyzed.

Monitoring the macrophage subset dynamics at single cell level

While TRAP-Seq provides valuable insights into gene expression patterns, it possesses inherent limitations in discerning variations between individual cellular subtypes. Specifically, alterations observed in bulk RNA-Seq data, like that from TRAP-Seq, can arise from either shifts in cell subtype proportions or genuine differential gene expression within a cell type. To circumvent this ambiguity and achieve a more granular understanding of cell subtype-specific changes, we employed scRNA-Seq on the aorta and adipose tissue using the same mouse model (Figure 1A). Immune cells were investigated from scRNA-Seq datasets generated using the 10x Genomics Chromium platform. Our analytical approach integrated data from both tissues to identify both common and tissue-specific subtypes, focusing on CD68 as a pan-myeloid marker. *Cd68*-expressing cells were selected based on their unique lineage marker gene expression profiles, distinguishing them from other immune cells (Supplementary Figures 5A-B and 6A; Supplementary Table 5). Our analysis identified 11 Cd68+ myeloid clusters,

ACCEPTED MANUSCRIPT

Downloaded from https://academic.oup.com/cardiovascres/advance-article/doi/10.1093/cvr/cvaf210/8316259 by Turku University Language Centre user on 10 November 2025

which were named based on one of a top marker gene (Figure 2A; Supplementary Figure 6B; Supplementary Table 6). This included six macrophage subtypes (*Trem2*+ lipid-associated [LAM], *Ccl3*+ proinflammatory, Retnla+ reparatory-like, *Cd163*+ resident, *Top2a*+ replicating, and *Ifit3*+ interferon (IFN)-activated macrophages), two monocyte subtypes (*Chil3*+ Ccr2-high and *Ace*+ Ccr2-low monocytes), and three dendritic cell subtypes (*Ifit8*+, *Cd209a*+, and *Siglech*+ dendritic cells) (Figure 2A). Adipose tissue displayed a wider myeloid cell spectrum than aorta (Figure 2B), and atherosclerosis increased the number of cells in all macrophage and monocyte clusters (Figure 2C) and several other immune cell types (Supplementary Figure 7A-B) in both tissues. Interestingly, while these subtypes illustrated a relatively gradual rise in the aorta, the adipose tissue marked a more distinct surge only during the advanced disease phase, highlighting temporal variations between tissues.

To evaluate the effect of tissue within the same transcriptomic cluster of cells, we concentrated on the three major macrophage clusters identified in both aorta and adipose tissues: Trem2+ (Lipid-associated), Ccl3+ (Chemokine program), and Cd163+ (Resident-like) macrophages (clusters 1, 2 and 4 in Figure 2A, with characteristic gene expression markers shown in Figure 2D).The results revealed that while many marker genes were shared between the tissues, a considerable amount were only detected in one tissue (Figure 2E; Supplementary Tables 7-8). For some of the tissue-specific marker genes, the expression difference between aorta and adipose macrophages within the same transcriptomic cluster) was substantial (Figure 2F). Notably, top tissue-differential genes pointed towards different types of lipids in aorta and adipose: cholesterol in aorta (*Abca1*, *Ch25h*) and fatty acid in adipose (*Fabp4*). Thus, marker variation within macrophage clusters may indicate distinct functional specialization, as has been described for resident macrophages in tissue homeostasis.[43]

ACCEPTED MANUSCRIPT

Downloaded from https://academic.oup.com/cardiovascres/advance-article/doi/10.1093/cvr/cvaf210/8316259 by Turku University Language Centre user on 10 November 2025

Given that our scRNA-Seq experiment lacked liver data, we additionally performed macrophage/monocyte scRNA-Seq data integration with a previously published liver dataset where HFD was fed for up to 36 weeks[16].The original authors classified monocytes and macrophages into 9 subtypes (Supplementary Figure 8A), and HFD duration considerably increased the fraction of LAM-s, monocyte-derived Kupffer cells (moKCs) and an intermediate 'mac1' population (Supplementary Figure 8B). Integration of monocytes and macrophages from aorta, adipose tissue and liver resulted in 9 clusters (Supplementary Figure 8C) and overlaying the original cell annotations revealed that cells are clustering by subtype rather than by tissue-of-origin (Supplementary Figure 8D). In the post-integration clusters, LAMs from all three tissues mostly grouped together (cluster 4), as did resident-like macrophages and Kupffer cells (cluster 1), proliferating macrophages (cluster 6), and two types of monocytes (clusters 5 and 2) (Supplementary Figure 8E). Chemokine and reparatory macrophages from adipose/aorta grouped with liver mac1, capsule macrophages and transitioning monocytes (cluster 0; Supplementary Figure 8E). For each of the 3 tissues, 3 clusters (0, 1, and 4) accounted for the majority (79-91%) of macrophages (Supplementary Figure 8F) and resembled the chemokine/inflammatory, resident-like, and lipid-associated subtypes, respectively (Supplementary Figure 8G), similarly to the subdivision found in adipose and aorta alone (Figure 2D-E). Using marker genes for each integrated cluster in each tissue (Supplementary Figure 8H, Supplementary Table 9), pathway enrichment analysis revealed that the transcriptomically-defined cell clusters tend to have similar enrichment profiles irrespective of tissue, supporting functional convergence across tissues (Supplementary Figure 8I, Supplementary Table 10). Finally, visualizing the common cluster markers (Supplementary Figure 8H) as gene set expression scores in the adipose–aorta–liver integrated UMAP highlights that these cluster gene programs exist as a continuum of activation levels, with areas

ACCEPTED MANUSCRIPT

Downloaded from https://academic.oup.com/cardiovascres/advance-article/doi/10.1093/cvr/cvaf210/8316259 by Turku University Language Centre user on 10 November 2025

of overlap (Supplementary Figure 8J). The importance of mixtures of programs was recently illustrated by the discovery of 'inflammatory LAMs' in human (but not mouse) plaques, with LAMs of other tissues remaining to be explored[8].

In aorta and adipose tissue scRNA-Seq, and in the external liver data[16], proliferating macrophages represented the fourth most abundant macrophage cluster (Supplementary Figure 8F) and appeared distinct from the rest of the macrophages (Supplementary Figure 8C). In the integrated dataset of aorta, adipose and liver macrophages, cell cycle phase scoring as well as individual cell cycle marker genes confirmed the clustering of cycling cells into a distinct group (Supplementary Figure 9A-B). Focusing on this cluster revealed a divergence into branches characterized by either LAM or resident-like macrophage markers (Supplementary Figure 9C), highlighting that while the replicating macrophage cluster is defined by cell cycle genes, the cells also express markers of non-cycling macrophage subtypes. By tissue, macrophages from adipose and aorta expressed LAM genes, whereas cycling macrophages in the liver expressed either LAM or resident markers (Supplementary Fig. 9D), suggesting that multiple macrophage subtypes undergo cell cycling in the liver, consistent with previous observations.[16]

ACCEPTED MANUSCRIPT

Downloaded from https://academic.oup.com/cardiovascres/advance-article/doi/10.1093/cvr/cvaf210/8316259 by Turku University Language Centre user on 10 November 2025

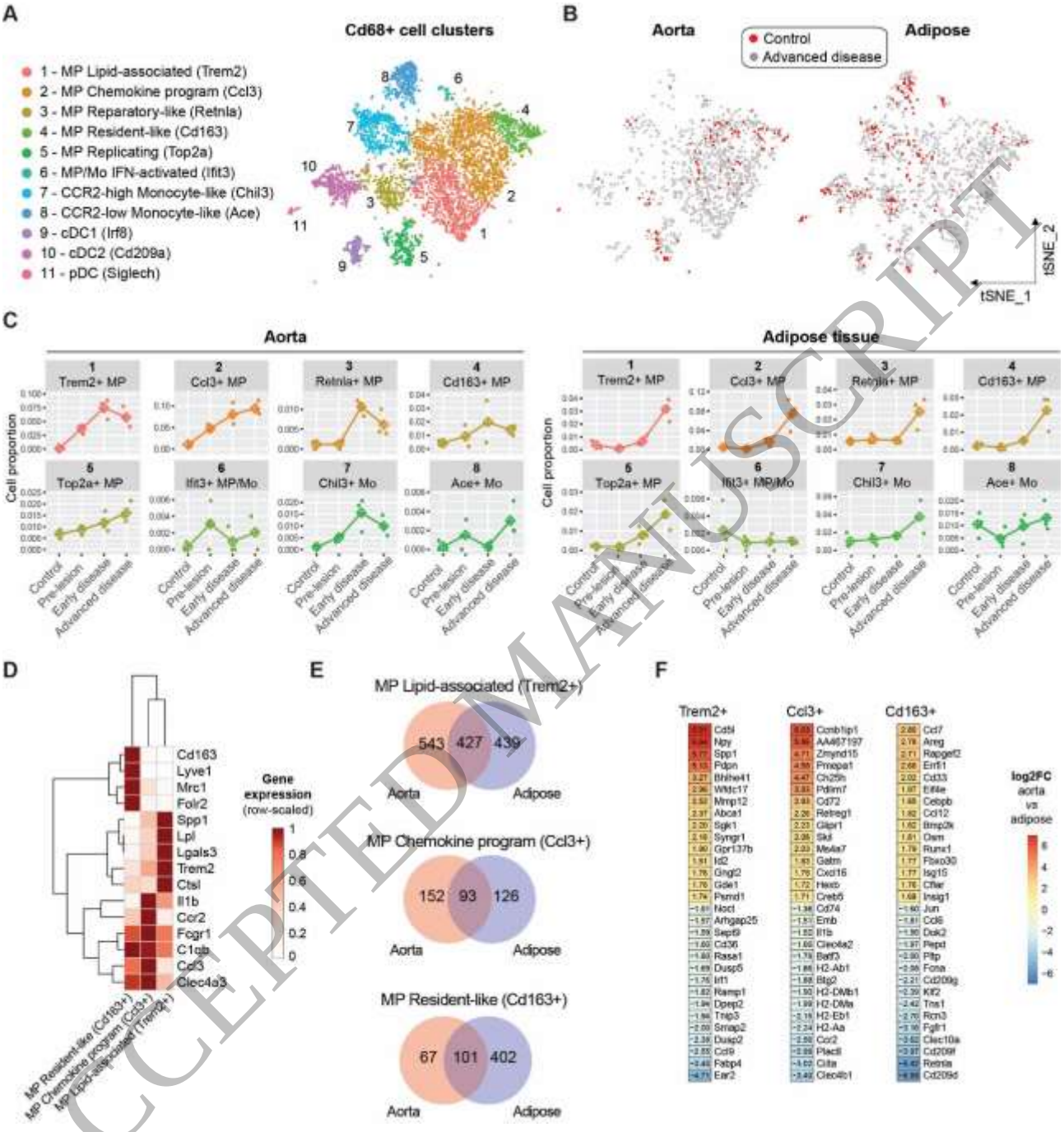

Figure 2. Clustering and monitoring of macrophage and monocyte changes during atherosclerosis progression in aorta and adipose tissue using scRNA-Seq. (A) tSNE projection of the scRNA-Seq profiles of Cd68+ myeloid cells represented as eleven manually annotated clusters from combined analysis of aorta and adipose tissue. **(B)** tSNE plot of Cd68+ myeloid cells specifically in the aorta and adipose tissue in control and advanced disease mice. **(C)** Relative changes in the cell state proportions during different stages of atherosclerosis shown for each of the three biological replicates in aorta and adipose tissue. **(D)** Gene expression of selected genes in the three most abundant macrophage clusters identified across aorta and adipose tissue. Pseudobulk gene expression (counts per million; CPM) was

ACCEPTED MANUSCRIPT

Downloaded from https://academic.oup.com/cardiovascres/advance-article/doi/10.1093/cvr/cvaf210/8316259 by Turku University Language Centre user on 10 November 2025

calculated per cluster across mouse aorta and adipose tissue scRNA-Seq cells. Gene expression is shown scaled per gene from 0 to 1 (maximum observed). **(E)** Number of marker genes detected as cluster markers in one or both tissues for the three most abundant macrophage subtypes shared between aorta and adipose tissue. **(F)** The most differential genes between aorta and adipose tissue amongst macrophages of the same cluster (markers from panel E). For the three most abundant macrophage clusters, the top tissue-specific genes are shown based on log2 fold change (log2FC) derived from pseudobulk gene expression analysis. Highly expressed genes were selected (at least 100 CPM in the higher expressing tissue). Positive log2FC denotes higher expression in aorta. For all panels, 3 mice per group were analyzed.

Identification of Trem2 as a circulating protein partly distinguishing between asymptomatic and symptomatic plaques

Next, we integrated the marker gene data from both TRAP-Seq and scRNA-Seq, with macrophage markers from human plaque scRNA-Seq [17], to pinpoint universal markers for disease-associated macrophages (Supplementary Table 11). Altogether, our analysis identified 388 macrophage enriched genes (Figure 3A) of which 70% (274/388) were further supported as macrophage-specific in the Human Protein Atlas body-wide scRNA-Seq atlas [44] (Supplementary Table 12). This list thus represents a comprehensive set of candidate genes for further exploration in macrophage biology and potential therapeutic intervention and diagnostic applications in atherosclerosis and related diseases. We subsequently directed our attention to membrane-bound receptor or metabolic proteins, given their potential as accessible diagnostic markers, facilitating cell type specific non-invasive disease detection and monitoring. Altogether 164 membrane proteins were identified, of which 54 represented receptors and 33 metabolic proteins (Figure 3A-B; Supplementary Table 12).

Among the receptor proteins, we identified *Trem2*, specifically associated with lipid-associated macrophages (LAMs) and exhibiting increased gene expression in atherosclerotic tissue (Figure 3C; Supplementary Figures 10 and 11A-B). *Trem2*+ LAMs have been previously observed in healthy human tissues as well as in pathological settings including atherosclerotic

ACCEPTED MANUSCRIPT

Downloaded from https://academic.oup.com/cardiovascres/advance-article/doi/10.1093/cvr/cvaf210/8316259 by Turku University Language Centre user on 10 November 2025

aorta [1,45], heart failure [46], adipose and liver tissue during obesity [47], damaged and fibrotic liver [48-50] and lung [51]. Recent studies have demonstrated that circulating soluble (s)TREM2 can act as an indicator of *Trem2*+ macrophage recruitment to fibrotic tissues in mouse models of metabolic dysfunction-associated fatty liver disease (MAFLD) [52,53]. In human patients, sTREM2 more accurately differentiated between the absence or presence of mild metabolic dysfunction-associated steatohepatitis (MASH) and its advanced stages than conventional liver disease-associated markers. Also, serum sTREM2 has been recently suggested to predict cardiovascular death [54]. Prompted by these findings, we sought to investigate whether sTREM2 could similarly function as a potential biomarker for atherosclerosis and potentially offer a means of distinguishing between patient subgroups, thereby facilitating patient stratification. Our results showed a robust and comparable increase in systemic sTREM2 levels in both in LDLR$^{-/-}$ApoB$^{100/100}$ and wild type mice upon HFD feeding (Figure 3D, left panel), confirming the prominent role of diet on sTREM2 levels [52]. Additionally, there was a mild but statistically significant increase in sTREM2 levels in LDLR$^{-/-}$ApoB$^{100/100}$ mice compared to wild type when both were fed a chow diet (Figure 3D, right panel).

A recent study from the Carotid Artery Risk for Atherosclerosis Study reported an association between elevated sTREM2 levels and carotid plaque progression [55]. To further investigate the underlying mechanisms and assess tissue-level expression of TREM2 in advanced human atherosclerosis, we evaluated its association with plaque burden in patients undergoing surgery for high-grade carotid stenosis and coronary artery disease. For this, we leveraged transcriptomic and proteomic data from two independent cohorts: the Biobank of Karolinska Endarterectomies (BiKE) [21-23] and the Stockholm-Tartu Atherosclerosis Reverse Network Engineering Task (STARNET) [24,25]. In line with *TREM2* gene expression in lesional macrophages, we observed significantly elevated TREM2 protein expression in carotid plaques

ACCEPTED MANUSCRIPT

Downloaded from https://academic.oup.com/cardiovascres/advance-article/doi/10.1093/cvr/cvaf210/8316259 by Turku University Language Centre user on 10 November 2025

compared to normal arteries (Figure 3E). Notably, our study extends previous findings [55] by showing that sTREM2 levels are significantly higher in symptomatic patients compared to asymptomatic individuals within the same cohort (Figure 3F). This suggests that beyond its expression in tissue, sTREM2 may serve as a clinically relevant biomarker of plaque instability and disease severity.

To further explore the systemic sources and correlates of circulating sTREM2, we assessed its relationship with tissue-level TREM2 expression in paired samples from early-stage lesions (mammary artery), advanced atherosclerosis (aorta), and liver. Plasma sTREM2 levels correlated significantly with TREM2 expression in all three tissues, with the strongest correlation observed in the liver (Figure 3G). Supporting a metabolic link, plasma sTREM2 levels positively correlated with lipid parameters including total cholesterol, LDL, HDL, and triglycerides, but not with CRP, a systemic inflammation marker (Figure 3H; Supplementary Figure 12). Together, these findings suggest that sTREM2 may reflect tissue-specific TREM2 protein level and associate it with lipid metabolism and plaque phenotype.

ACCEPTED MANUSCRIPT

Downloaded from https://academic.oup.com/cardiovascres/advance-article/doi/10.1093/cvr/cvaf210/8316259 by Turku University Language Centre user on 10 November 2025

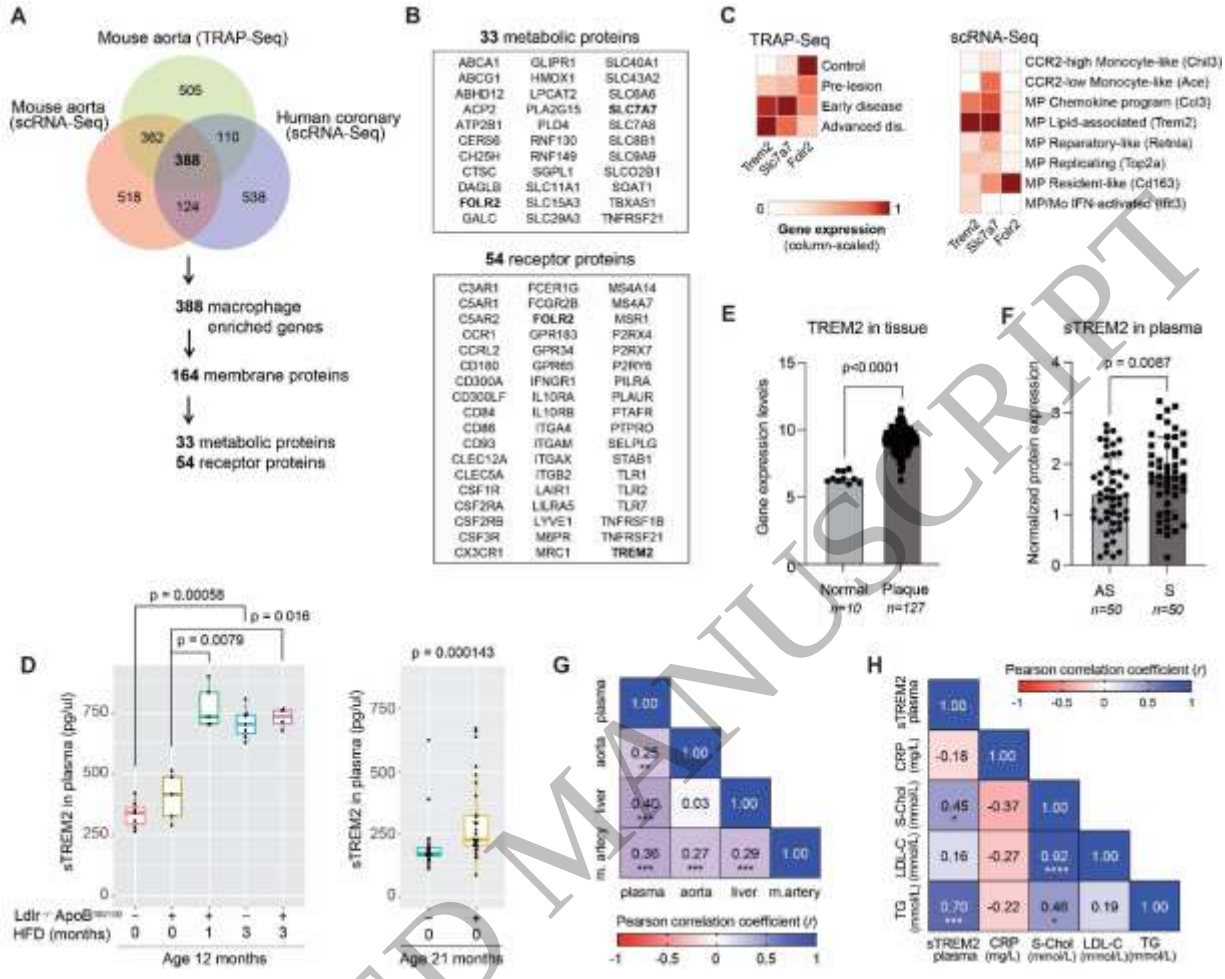

Figure 3. Comparative analysis of gene expression and sTREM2 levels in mouse and human samples. (A) Venn diagram illustrating the overlap of gene expression profiling results from mouse aorta samples analyzed by TRAP-Seq and scRNA-Seq, and human coronary arteries analyzed by scRNA-Seq, revealing a subset of genes enriched in macrophages. The analysis identifies 388 macrophage-enriched genes, of which 164 are membrane proteins, 33 are metabolic proteins, and 54 are receptor proteins. Sample sizes: TRAP-Seq n = 6 mice, mouse scRNA-Seq n = 3 mice, and human scRNA-Seq n = 4 patients. **(B)** Detailed lists of identified proteins categorized into metabolic proteins and receptor proteins from A. **(C)** Expression of *Trem2*, *Slc7a7* and *Folr2* in TRAP-Seq and scRNA-Seq of mouse aorta. For TRAP-Seq, values represent the average transcripts per million across IP replicates, while for scRNA-Seq, they correspond to cluster pseudobulk counts per million. Gene expression for each method is scaled per gene from 0 to 1, with 1 representing the maximum observed expression. Sample sizes are as indicated in panel A. **(D)** Quantification of soluble (s)TREM2 in the plasma of mice carrying (+) or not carrying (-) the hypercholesterolemic LDLR$^{-/-}$ ApoB$^{100/100}$ mutations. The mice were subjected to either a regular diet (0) or a high-fat diet (HFD) for 1 or 3 months. Data are presented for both 12-month-old and 21-month-old mice, illustrating the impact of diet and age. The Wilcoxon rank sum test was used for comparing groups. Sample size (mice per group) at 12 months was 7 (-; HFD 0), 5 (+; HFD 0), 5 (+; HFD 1), 7 (-; HFD 3) and 4 (+; HFD 3), and at 21 months was 25 (-) and 30 (+). **(E-F)** Normalized

ACCEPTED MANUSCRIPT

Downloaded from https://academic.oup.com/cardiovascres/advance-article/doi/10.1093/cvr/cvaf210/8316259 by Turku University Language Centre user on 10 November 2025

protein expression (NPX) levels of TREM2 in (**E**) human atherosclerotic tissue and (**F**) plasma from individuals of the BiKE cohort in individuals with asymptomatic (AS) and symptomatic (S) carotid stenosis. NPX was calculated as recommended by Olink and is on a $\log_2$ scale in arbitrary units (one NPX difference corresponds to 2-fold in protein concentration). Each dot represents an individual patient's sTREM2 levels, with 50 patients in each group. Statistical significance was measured using a two-sided Student's t-test with unequal variance. (**G**) Heatmap of Pearson correlation coefficients between plasma and tissue TREM2 levels (atherosclerotic aortic arterial wall = aorta, liver, and mammary artery = m.artery) in 165 coronary artery disease patients from the STARNET cohort. (**H**) Pearson correlation matrix showing relationships between plasma sTREM2, C-reactive protein (CRP), serum cholesterol (S-Chol), low-density lipoprotein cholesterol (LDL-C), and triglycerides (TG) in 20 individuals from the BiKE cohort. For both panels, the color scale represents the Pearson correlation coefficient (r), ranging from –1 to +1. Asterisks denote statistical significance: *p < 0.05, **p < 0.01, ***p < 0.001, ****p < 0.0001.

Exploiting folate and glutamine transport to trace atherosclerosis progression using PET

We next sought to identify potential biomarkers that could act as PET tracers, allowing for non-invasive imaging and real-time monitoring of disease progression in the spatial context. We identified folate receptor beta (*Folr2*; *FR-β*) and solute carrier family 7 member 7 (*Slc7a7),* which are especially promising receptors/transporters because their substrates, folate (FOL) and glutamine (Gln) respectively, can be readily radiolabeled for PET investigation. *Slc7a7* expression was most strongly associated with lipid-associated macrophages (LAMs), while *Folr2* represents a marker of resident macrophages (Figure 3C). The macrophage-specific expression of these genes was confirmed via immunohistochemical staining of the aortic root sections of atherosclerotic mice (Supplementary Figure 10) and scRNA-Seq of human and mouse atherosclerosis (Supplementary Figure 11A-B). The expression levels of *SLC7A7* and *FOLR2* were significantly elevated in human atherosclerotic plaques compared to normal tissue, and were also mildly but significantly increased in symptomatic patients *vs.* asymptomatic patients within the BiKE cohort (Supplementary Figure 13A-B).

ACCEPTED MANUSCRIPT

Downloaded from https://academic.oup.com/cardiovascres/advance-article/doi/10.1093/cvr/cvaf210/8316259 by Turku University Language Centre user on 10 November 2025

We investigated the uptake of ^{18}F-FGln and ^{68}Ga-FOL in comparison to the widely used tracer, ^{18}F-FDG, across the three disease stages in LDLR$^{-/-}$ApoB$^{100/100}$ mice (mouse characteristics summarized in Supplementary Table 13). PET/CT images of advanced disease showed uptake of ^{18}F-FGln and ^{68}Ga-FOL in aortic arch, while with ^{18}F-FDG aortic arch uptake was poorly resolved due to high physiological myocardial uptake (Figure 4A). To specifically quantify aortic arch uptake while accounting for radioactivity residing in blood, we calculated a target-to-background ratio (TBR) comparing aortic arch to vena cava as a representation of the background signal of blood. The average TBR of ^{68}Ga-FOL in the aortic arch was significantly higher in both early disease ($P = 0.04$) and advanced disease ($P = 0.008$) compared to prelesion stage (Figure 4B). Similarly, the TBR of ^{18}F-FGln in the aortic arch showed higher tendency in early disease and advanced disease compared to prelesion stage, although statistical significance was not reached. Likewise, the TBR of ^{18}F-FDG in the aortic arch showed a trend of higher values in early and advanced disease compared to prelesion stage without a statistically significant difference. *Ex vivo* gamma counting, using whole aorta rinsed clean of blood, confirmed the results of *in vivo* PET data (Supplementary Figure 14A).

ACCEPTED MANUSCRIPT

Downloaded from https://academic.oup.com/cardiovascres/advance-article/doi/10.1093/cvr/cvaf210/8316259 by Turku University Language Centre user on 10 November 2025

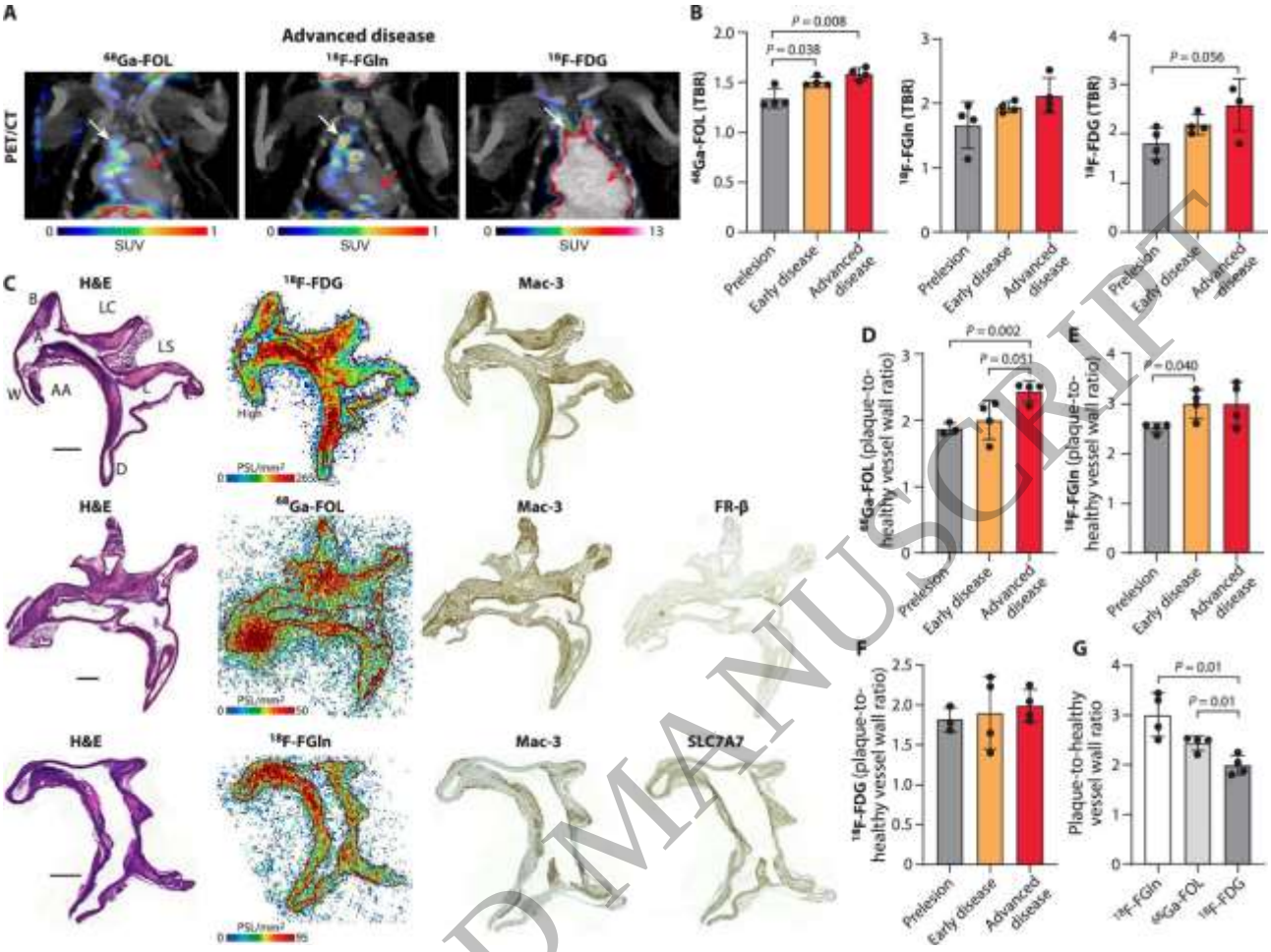

Figure 4. PET studies in mice. (**A**) Representative coronal PET/CT images of mice with advanced atherosclerosis using ^{68}Ga-FOL,^{18}F-FGln or ^{18}F-FDG. White arrows indicate the aortic arch and red arrows indicate the myocardium. SUV, standardized uptake value. Group size: as in panel B. (**B**) Quantification of *in vivo* PET/CT tracer uptake in the aortic arch expressed as target-to-background ratio (TBR = $SUV_{max,\ aortic\ arch}/SUV_{mean,\ blood}$, at 40–60 minutes post-injection) Values are mean ± SD (n = 4 mice), except in advanced disease group with ^{18}F-FDG (n = 3 mice). (**C**) Representative images of hematoxylin–eosin (H&E) staining, autoradiographs, Mac-3 macrophage staining, FR-β and SLC7A7 glutamine transporter staining of consecutive aorta cryosections from a mouse with advanced disease. Black outline sketch denote the plaque region. Scale bar = 500 µm. A = arch; AA = ascending aorta; B = brachiocephalic artery; D = descending thoracic aorta; L = lesion; LC = left common carotid artery; LS = left subclavian artery; W = vessel wall. PSL/mm^2, photostimulated luminescence per square millimeter. Group size: as in panels D-F. (**D-F**) Quantification of autoradiography data expressed as plaque-to-healthy vessel wall ratio. Values are mean ± SD (n = 4 mice), except in prelesion group with ^{68}Ga-FOL and ^{18}F-FDG (n = 3 mice). (**G**) Quantification of autoradiography data from advanced disease group expressed as plaque-to-healthy vessel wall ratio showing difference between the tracers. Values are mean ± SD (n = 4 mice). *P*-values were calculated using a two-tailed unpaired Student's *t* test.

ACCEPTED MANUSCRIPT

Downloaded from https://academic.oup.com/cardiovascres/advance-article/doi/10.1093/cvr/cvaf210/8316259 by Turku University Language Centre user on 10 November 2025

The myocardial uptake of ^{18}F-FDG and ^{68}Ga-FOL increased during the development of the disease while no difference in the myocardial uptake of ^{18}F-FGln was observed between the disease groups (Supplementary Figure 14B). However, in the advanced disease, the myocardial uptake of ^{18}F-FGln and ^{68}Ga-FOL (both $P < 0.001$) were significantly lower compared to ^{18}F-FDG, and the uptake of ^{68}Ga-FOL was significantly lower ($P < 0.01$) than that of ^{18}F-FGln (Supplementary Figure 14B). The uptake of the tracers in other tissues determined by *ex vivo* gamma counting is listed in Supplementary Tables 14-16.

To investigate the precise localization of the tracers uptake in the aorta, a comparative analysis was performed by examining autoradiographs with adjacent histological and immunohistochemical staining. The analysis demonstrated a localization of ^{68}Ga-FOL, ^{18}F-FGln and ^{18}F-FDG uptake in macrophage-rich lesions in line with the expression profiles of FR-β and SLC7A7 (Figure 4C). Especially plaque ^{18}F-FGln uptake was clearly higher compared to vessel wall and adventitia in all disease groups (Supplementary Figure 14C and Supplementary Table 17). The plaque-to-healthy vessel wall ratio of ^{68}Ga-FOL was significantly higher in advanced disease compared to early disease ($P = 0.05$) and prelesion stage ($P = 0.002$, Figure 4D). The plaque-to-healthy vessel wall ratio of ^{18}F-FGln was significantly higher in early disease ($P = 0.04$) but not in advanced disease compared to prelesion stage (Figure 4E). The plaque-to-healthy vessel wall ratio of ^{18}F-FDG was similar in all disease stages (Figure 4F). In advanced disease, the plaque-to-healthy vessel wall ratio of ^{18}F-FGln and ^{68}Ga-FOL were significantly higher compared to ^{18}F-FDG (Figure 4G). Collectively, these findings indicate that both ^{18}F-FGln and ^{68}Ga-FOL are promising non-invasive markers that reflect the atherosclerotic burden within the vessels.

ACCEPTED MANUSCRIPT

Downloaded from https://academic.oup.com/cardiovascres/advance-article/doi/10.1093/cvr/cvaf210/8316259 by Turku University Language Centre user on 10 November 2025

Slc7a7 contributes to foam cell phenotype

The *Slc7a7* gene encodes for a protein that is part of an amino acid transporter system. Specifically, it is a component of the y+L amino acid transport system, which is involved in the transport of cationic amino acids (efflux from the cell) in exchange of large neutral amino acids with sodium (influx into the cell) across the plasma membrane, Gln being one of the preferred neutral amino acid substrates [56,57]. Among the reported glutamine transporters, scRNA-Seq of the mouse aorta revealed that *Slc7a7* exhibited a tendency for co-expression with *Trem2* (Supplementary Figure 11A), whereas *Slc7a8* was more broadly expressed in macrophages (Supplementary Figure 15). In contrast, the glutamine transporters *Slc1a5*, *Slc38a1*, *Slc38a2*, and *Slc3a2* were ubiquitously expressed across all cell types within the mouse plaque (Supplementary Figure 15). In human coronary artery scRNA-Seq, *SLC7A7* was also specific to macrophages as a cell type, but its expression covered both *TREM2*-positive and -negative subpopulations (Supplementary Figure 11B). Dysfunctional mutations in *Slc7a7* gene lead to lysinuric protein intolerance, a rare metabolic disorder that results from defective transport of cationic amino acids [58]. The *Slc7a7* knockout mouse model recapitulates this phenotype [59]. However, despite these findings, the understanding of *Slc7a7*'s role in macrophages is still limited. Notably, *Slc7a7* has been identified as crucial for macrophage viability and efferocytosis in zebrafish [60]. While it promotes an anti-inflammatory state in cultured macrophages [61], its role in lipid loading associated with LAMs remains uncharacterized. To investigate this, we differentiated bone marrow-derived macrophages from myeloid-specific (LysM-Cre) *Slc7a7* knockout mice (*Slc7a7*$^{LysM-/-}$), which exhibited a 73-88% reduction in *Slc7a7* expression compared to control mice (*Slc7a7*$^{LysM+/+}$; Supplementary Figure 16). We then exposed control and *Slc7a7*$^{LysM-/-}$ macrophages to acetylated LDL (Ac-LDL) and oxidized LDL (Ox-LDL) to assess foam cell formation and to identify global changes in gene expression. In wild type cells,

ACCEPTED MANUSCRIPT

Downloaded from https://academic.oup.com/cardiovascres/advance-article/doi/10.1093/cvr/cvaf210/8316259 by Turku University Language Centre user on 10 November 2025

both forms of LDL upregulated *Slc7a7* mRNA expression (Supplementary Figure 16). Oil Red O staining results indicated impaired Ox-LDL uptake in *Slc7a7*$^{LysM-/-}$ bone marrow-derived macrophages compared to wild type (Figure 5A-B). No difference was evident between the genotypes for Ac-LDL uptake, potentially due to the considerably lower overall uptake signal of Ac-LDL in this experiment (Figure 5B). Based on RNA-Seq, deletion of *Slc7a7* attenuated the transcriptional signature associated with LAMs in both Ac-LDL and Ox-LDL treatments (Figure 5C). Finally, in a bone marrow transplantation experiment, LDLR-deficient mice that received *Slc7a7*$^{LysM-/-}$ bone marrow showed a trend (P = 0.052) towards reduced glutamine uptake in aorta after 11 weeks of HFD, relative to recipients of *Slc7a7*$^{LysM+/+}$ bone marrow (Figure 5D). Plasma cholesterol and triglyceride levels showed no significant differences between the groups (cholesterol: *Slc7a7*$^{LysM+/+}$ 485.8 mg/dL, *Slc7a7*$^{LysM-/-}$ 532.3 mg/dL, P = 0.26; triglycerides: *Slc7a7*$^{LysM+/+}$ 76.4 mg/dL, *Slc7a7*$^{LysM-/-}$ 77.2 mg/dL, P = 0.91), indicating that the observed results were not influenced by lipid levels. Collectively, these findings indicate that the loss of *Slc7a7* impedes lipid uptake in macrophages and suggests a significance of glutamine metabolism in foam cell formation.

ACCEPTED MANUSCRIPT

Downloaded from https://academic.oup.com/cardiovascres/advance-article/doi/10.1093/cvr/cvaf210/8316259 by Turku University Language Centre user on 10 November 2025

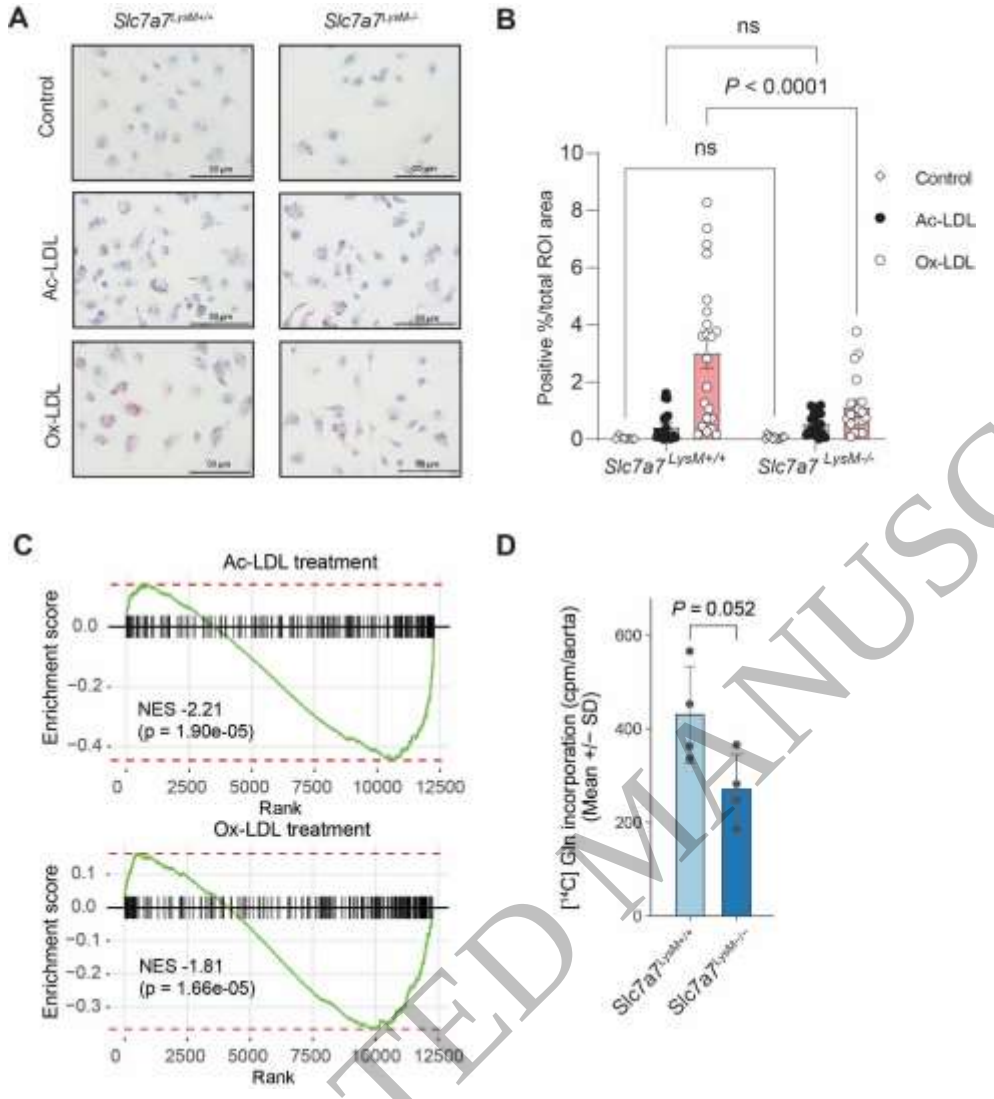

Figure 5. Evaluation of lipoprotein uptake and gene expression in *Slc7a7* knockout macrophages. (A) Histological analysis of macrophage uptake of lipoproteins in Slc7a7 knockout and wild type mice. Images depict bone-marrow derived macrophages (BMDM-s) from control, acetylated LDL (Ac-LDL), and oxidized LDL (Ox-LDL) treated groups for both in *Slc7a7*$^{LysM+/+}$ (wild type) and *Slc7a7*$^{LysM-/-}$ (knockout) mice. Images are representative of typical results of BMDM-s generated from 3 mice per genotype. Scale bar: 50 µm. **(B)** Quantification of positive ROI (region of interest) area comparing control, Ac-LDL, and Ox-LDL treatments in *Slc7a7*$^{LysM+/+}$ and *Slc7a7*$^{LysM-/-}$ macrophages. Each dot represents an individual sample measurement, with the horizontal line indicating the mean and error bars representing standard deviation. The number of measurements for *Slc7a7*$^{LysM+/+}$ and *Slc7a7*$^{LysM-/-}$, respectively, was 8 and 11 (Control), 19 and 19 (Ac-LDL), and 22 and 19 (Ox-LDL). Statistical significance is denoted as "ns" (not significant) or by p-value (Two-way ANOVA followed by Šídák's multiple comparisons test). **(C)** Gene set enrichment analysis (GSEA) comparing expression of the lipid-associated macrophage gene signature between *Slc7a7*$^{LysM-/-}$ and *Slc7a7*$^{LysM+/+}$ BMDM-s (n = 3 per genotype) subjected to either Ac-LDL or Ox-LDL treatment. The plots illustrate the normalized enrichment score (NES) and the associated p-values, reflecting the degree to which

ACCEPTED MANUSCRIPT

Downloaded from https://academic.oup.com/cardiovascres/advance-article/doi/10.1093/cvr/cvaf210/8316259 by Turku University Language Centre user on 10 November 2025

the genes are overrepresented at the top or bottom of the ranked gene list. The green line represents the running enrichment score (ES) for the gene set as the analysis walks down the ranked list. The black bars indicate the position of gene set members in the ranked list of genes. The red dashed lines indicate the threshold for significance, with gene sets showing enrichment at the top (positive ES) or bottom (negative ES) of the ranked list. **(D)** [^{14}C]glutamine incorporation in aortas from Ldlr$^{-/-}$ mice transplanted with bone marrow from either *Slc7a7*$^{LysM+/+}$ or *Slc7a7*$^{LysM-/-}$ mice and fed an atherogenic diet for 11 weeks. Data from individual mice are presented (n = 4 mice per group) and summarized as the mean ± S.D (cpm, counts per minute). Two-tailed Student's t-test was used for statistical analysis.

DISCUSSION

Macrophages play a major role in the pathogenesis of atherosclerosis. The recent development and rapid progress of single-cell technologies have enabled comprehensive mapping of the wide range of cell types and their phenotypes present in atherosclerotic plaques, including comparison between mouse and human[4,5]. These studies have identified three main macrophage populations within atherosclerotic plaques including proinflammatory, LAM and resident macrophages [1]. A better understanding of the cell phenotype and function of atherosclerosis-associated populations, along with their correlation with disease progression, clinical features, and future events, may help guide future strategies to predict and mitigate atherosclerosis complications. To this end, we provide a comprehensive identification of disease associated macrophages in three major tissues implicated in the pathogenesis of atherosclerosis. We identified a signature of 388 genes that are shared across both mouse and human plaques. Among them, 164 represent membrane-bound receptor or metabolic proteins, making them amenable for non-invasive disease detection and monitoring.

Trem2+ LAMs have been shown to be widely distributed across healthy and diseased human tissues [62]. TREM2, a membrane protein expressed on immune cells, has been implicated in both neurodegenerative diseases and cancer, with studies suggesting therapeutic potential in targeting its activity [63,64]. In line with this, the cerebrospinal fluid levels of sTREM2

ACCEPTED MANUSCRIPT

Downloaded from https://academic.oup.com/cardiovascres/advance-article/doi/10.1093/cvr/cvaf210/8316259 by Turku University Language Centre user on 10 November 2025

have been associated with Alzheimer's disease [65], whereas recently also serum levels of sTREM2 have been associated with MASH [52] and cardiovascular death [54]. In this study, we provide evidence that sTREM2 levels are also correlated with plaque vulnerability, notably exhibiting a heightened capacity to distinguish symptomatic patients from asymptomatic. Importantly, tissue TREM2 levels in early and advanced lesions, and particularly in the liver, showed significant correlations with plasma levels, suggesting that circulating sTREM2 may serve as a proxy for underlying tissue-specific changes. Supporting the liver's role in this axis, plasma sTREM2 levels also correlated with cholesterol and triglyceride levels, a finding supported by a recent study analyzing plasma proteins in a cohort of 35,000 Icelanders [66]. This pattern suggests a complex interplay between sTREM2 and lipid metabolism, as well as inflammatory processes in the body and motivates future studies to explore the relationship between sTREM2 and tissue lipid content Mouse studies investigating the role of TREM2 in atherosclerosis (recently reviewed in [67]) have shown that hematopoietic or global TREM2 deficiency enhances necrotic core formation in early atherosclerosis, whereas TREM2 agonism reduces it [55]. However, this effect appears to be model-dependent, as another study reported that macrophage-specific TREM2 deficiency led to reduced lesion formation [68]. Additionally, TREM2 agonist antibody was shown to improve plaque stability by promoting macrophage survival, smaller necrotic core and greater collagen deposition [69]. These findings also suggest that modulating TREM2 activity could be a promising strategy for improving cardiovascular outcomes in patients with elevated lipid levels and inflammatory markers.

Traditional imaging methods like computed tomography (CT) and magnetic resonance (MR) mainly offer anatomical insights with limited biochemical and functional data. PET imaging, however, offers precise biochemical quantification, high sensitivity, and clinical adaptability, making it a preferred method for tracking inflammation in CVDs [70,71]. The

ACCEPTED MANUSCRIPT

Downloaded from https://academic.oup.com/cardiovascres/advance-article/doi/10.1093/cvr/cvaf210/8316259 by Turku University Language Centre user on 10 November 2025

predominantly used PET tracer is ^{18}F-FDG, which, despite its widespread use and availability, has drawbacks. As a glucose analog, it is accumulating in metabolically active tissues such as myocardium, causing background noise[72]. ^{18}F-FDG's effectiveness can also be influenced by fasting, blood glucose, insulin levels, and certain drugs, making it less suitable for diabetic patients with hyperglycemia[73]. To address this limitation, we have previously described the radiosynthesis of ^{18}F-FGln and ^{68}Ga-FOL and demonstrated lower myocardial uptake compared ^{18}F-FDG[27,28]. Here, this analysis was extended to provide a more detailed time course analysis of the accumulation of resident (^{68}Ga-FOL) and LAM (^{18}F-FGln) macrophages. Our analysis demonstrated that both tracers reflect the disease associated macrophage burden with minor differences in the dynamics. Specifically, ^{18}F-FGln demonstrated slightly higher accumulation and plaque-to-healthy wall ratio during the early disease stages compared to ^{68}Ga-FOL, indicating temporal variations between the two. Although the overall target-to-background ratio for ^{18}F-FGln was higher, ^{68}Ga-FOL showed more promise in detecting early disease and differentiating between mid and advanced stages, as the difference between the disease and pre-disease states with 18F-FGln was not significant. We acknowledge that the small sample sizes in this study limit the statistical power regarding temporal differences between tracers, and larger studies are needed to validate these findings.

Glutamine has been shown to affect macrophage polarization, where high glutamine uptake and glutaminolysis are associated with an anti-inflammatory and efferocytic phenotype [35,74,75]. Notably, around one-third of the carbon in tricarboxylic acid (TCA) metabolites and more than half of the nitrogen in uridine diphosphate *N*-acetylglucosamine (UDP-GlcNAc) synthesis in M2-like macrophages originates from glutamine, emphasizing its critical role in macrophage polarization. In line with this, transient glutamine deprivation has been observed to adversely impact the M2 activation program. Previous *in vitro* studies have proposed that enhanced

ACCEPTED MANUSCRIPT

Downloaded from https://academic.oup.com/cardiovascres/advance-article/doi/10.1093/cvr/cvaf210/8316259 by Turku University Language Centre user on 10 November 2025

glutamine accumulation could be due to increased expression of a glutamine transporter, *Slc1a5* [75]. Macrophages express multiple glutamine transporters, including *Slc1a5*, *Slc3a2*, *Slc38a1*, and *Slc38a2*—also found in other plaque cell types— and *Slc7a7*, which is restricted to macrophages. Our studies also support that *Slc7a7* contributes to macrophage foam cell formation and expression of the LAM gene signature. This aligns with the requirement of Slc7a7 for efferocytosis and the maintenance of an anti-inflammatory state in macrophages[60,61], as well as findings from patients with *SLC7A7* mutations, which results in altered inflammatory responses and impaired phagocytosis by macrophages[76,77]. While our findings highlight the importance of *Slc7a7*, further research should include other ubiquitously expressed glutamine transporters to fully understand the role of glutamine metabolism in atherosclerosis.

In conclusion, our findings present a novel set of potential biomarkers for atherosclerosis. Considering the pivotal role of macrophages in atherosclerosis, PET imaging offers a non-invasive means to quantify specific disease markers. When integrated with genetic screening results and liquid biopsy biomarker data, this approach holds potential for formulating personalized therapeutic interventions. Additionally, it could be instrumental in refining patient selection for immunotherapy and facilitating its subsequent monitoring. We anticipate that the macrophage markers we have identified will deepen our understanding of the pathophysiology underlying atherosclerosis and guide future research endeavors.

Acknowledgements

We acknowledge Single Cell Genomics Core, Genome Center and Bioinformatics Center at University of Eastern Finland, Finnish Functional Genomics Centre and Biocenter Finland for infrastructure support. The authors thank Aake Honkaniemi (Turku PET Centre), Erica Nyman, Marja-Riitta Kajaala (Histology Core Facility of the Institute of Biomedicine, University of Turku,

ACCEPTED MANUSCRIPT

Downloaded from https://academic.oup.com/cardiovascres/advance-article/doi/10.1093/cvr/cvaf210/8316259 by Turku University Language Centre user on 10 November 2025

Finland), Timo Kattelus and Tuula Salonen for technical assistance. We thank Prof. Jason Lewis and Dr. Ouathek Ouerfelli at the Memorial Sloan Kettering Cancer Center for providing the ^{18}F-FGln precursor. The ^{18}F-FGln precursor tosylate and FGln reference standard were synthesized by the Organic Synthesis Core Facility at Memorial Sloan Kettering Cancer Center, New York. Funding for the Core Facility is provided by grant NCI R50 CA243895-01 and by an NCI P30 CA008748-53 Core Grant. We thank the EMBL GeneCore for assisting in bulk RNA-Seq experiments. The authors also acknowledge the Human Disease Blood Atlas/ Human Protein Atlas for performing plasma Olink analyses in BiKE.

Funding

This study was funded by the European Research Council (ERC) under the European Union's Horizon 2020 research and innovation program (Grant No. 802825 to M.U.K), Research Council of Finland (Grants Nos. 314556 and 335975 to A.Ro, 333021 and 335973 to M.U.K, 352968 to T.Ö and M.T, 335964 to M.H, 350049 to A-K.R), Finnish Foundation for Cardiovascular Research (A-K.R, A.Ro, M.U.K), Sigrid Juselius Foundation (A.S, A.Ro and M.U.K), Spanish Ministry of Science and Innovation (PID2021-122802OB-I00 to M.P and S.B), Jane and Aatos Erkko Foundation (to A.R.), Finnish Cultural Foundation (to S.P.), Turku University Foundation (to S.P.), Orion Research Foundation (to A-K.R.), the ANR (grants 20-CE14-CHIC and 24-CE14-Glutacare to L.Y.C), and the University of Eastern Finland Doctoral Program of Molecular Medicine. A.Ra was supported by the Genomics and Mechanisms in Translational Medicine (GenomMed) Doctoral Programme, cofunded by the Horizon 2020 Framework Programme of the European Union, Marie Skłodowska-Curie grant agreement no. 740264. This research was supported by InFLAMES Flagship Programme of the Research Council of Finland (decision number: 337530). J.L.M.B. acknowledges support from the

ACCEPTED MANUSCRIPT

Downloaded from https://academic.oup.com/cardiovascres/advance-article/doi/10.1093/cvr/cvaf210/8316259 by Turku University Language Centre user on 10 November 2025

Swedish Research Council (2018-02529 and 2022-00734), the Swedish Heart Lung Foundation (2017-0265 and 2020-0207), the Leducq Foundation AtheroGen (22CVD04) and PlaqOmics (18CVD02) consortia; the National Institute of Health-National Heart Lung Blood Institute (NIH/NHLBI, R01HL164577; R01HL148167; R01HL148239, R01HL166428, and R01HL168174), American Heart Association Transformational Project Award 19TPA34910021, and from the CMD AMP fNIH program. L.M. is the recipient of fellowships and awards from the Swedish Research Council [VR, 2023-02724, 2019-02027], Karolinska Institute Consolidator program, Swedish Heart-Lung Foundation [HLF, 20240094, 20230357, 20210466, 20200621, 20200520, 20180244, 20180247, 201602877] and Swedish Society for Medical Research [SSMF, P13-0171]. L.M. also acknowledges funding from Mats Kleberg's, Sven and Ebba-Christina Hagberg's, Tore Nilsson's, Magnus Bergvall's and Karolinska Institute research (KI Fonder) and doctoral education (KID) foundations. The work of L.M. was also funded by a research grant from the European Union's Horizon Europe program under grant agreement No 101136962 (NextGen). Project funding was also obtained by U.H. from the Swedish Heart-Lung Foundation (20180036, 20170584), the Swedish Research Council (2017-01070, 2019-02027), and King Gustav Vth and Queen Victoria's Foundation.

References

1. Willemsen L, de Winther MP. Macrophage subsets in atherosclerosis as defined by single-cell technologies. J Pathol. 2020;250(5):705-14.
2. Gainullina A, Mogilenko DA, Huang LH, Todorov H, Narang V, Kim KW, et al. Network analysis of large-scale ImmGen and Tabula Muris datasets highlights metabolic diversity of tissue mononuclear phagocytes. Cell Rep. 2023;42(2):112046.
3. Gautier EL, Shay T, Miller J, Greter M, Jakubzick C, Ivanov S, et al. Gene-expression profiles and transcriptional regulatory pathways that underlie the identity and diversity of mouse tissue macrophages. Nat Immunol. 2012;13(11):1118-28.
4. de Winther MPJ, Back M, Evans P, Gomez D, Goncalves I, Jorgensen HF, et al. Translational opportunities of single-cell biology in atherosclerosis. Eur Heart J. 2023;44(14):1216-30.

ACCEPTED MANUSCRIPT

Downloaded from https://academic.oup.com/cardiovascres/advance-article/doi/10.1093/cvr/cvaf210/8316259 by Turku University Language Centre user on 10 November 2025

5. Horstmann H, Michel NA, Sheng X, Hansen S, Lindau A, Pfeil K, et al. Cross-species single-cell RNA sequencing reveals divergent phenotypes and activation states of adaptive immunity in human carotid and experimental murine atherosclerosis. Cardiovasc Res. 2024;120(14):1713-26.
6. Polkinghorne MD, West HW, Antoniades C. Adipose Tissue in Cardiovascular Disease: From Basic Science to Clinical Translation. Annu Rev Physiol. 2024;86:175-98.
7. Adam CA, Salaru DL, Prisacariu C, Marcu DTM, Sascau RA, Statescu C. Novel Biomarkers of Atherosclerotic Vascular Disease-Latest Insights in the Research Field. Int J Mol Sci. 2022;23(9).
8. Dib L, Koneva LA, Edsfeldt A, Zurke Y-X, Sun J, Nitulescu M, et al. Lipid-associated macrophages transition to an inflammatory state in human atherosclerosis, increasing the risk of cerebrovascular complications. Nature Cardiovascular Research. 2023;2(7):656-72.
9. Sriranjan RS, Tarkin JM, Evans NR, Le EPV, Chowdhury MM, Rudd JHF. Atherosclerosis imaging using PET: Insights and applications. Br J Pharmacol. 2021;178(11):2186-203.
10. Shibata N, Carlin AF, Spann NJ, Saijo K, Morello CS, McDonald JG, et al. 25-Hydroxycholesterol activates the integrated stress response to reprogram transcription and translation in macrophages. J Biol Chem. 2013;288(50):35812-23.
11. Ali Khan A, Valera Vazquez G, Gustems M, Matteoni R, Song F, Gormanns P, et al. INFRAFRONTIER: mouse model resources for modelling human diseases. Mamm Genome. 2023;34(3):408-17.
12. Ord T, Lonnberg T, Nurminen V, Ravindran A, Niskanen H, Kiema M, et al. Dissecting the polygenic basis of atherosclerosis via disease-associated cell state signatures. Am J Hum Genet. 2023;110(5):722-40.
13. de Sande AH, Turunen T, Bouvy-Liivrand M, Örd T, Palani S, Tundidor-Centeno C, et al. Cell-type-specific characterization of miRNA gene dynamics in immune cell subpopulations during aging and atherosclerosis disease development at single-cell resolution. bioRxiv. 2023:2023.10.09.561173.
14. Stuart T, Butler A, Hoffman P, Hafemeister C, Papalexi E, Mauck WM, 3rd, et al. Comprehensive Integration of Single-Cell Data. Cell. 2019;177(7):1888-902 e21.
15. Yang S, Corbett SE, Koga Y, Wang Z, Johnson WE, Yajima M, et al. Decontamination of ambient RNA in single-cell RNA-seq with DecontX. Genome Biol. 2020;21(1):57.
16. Remmerie A, Martens L, Thone T, Castoldi A, Seurinck R, Pavie B, et al. Osteopontin Expression Identifies a Subset of Recruited Macrophages Distinct from Kupffer Cells in the Fatty Liver. Immunity. 2020;53(3):641-57 e14.
17. Wirka RC, Wagh D, Paik DT, Pjanic M, Nguyen T, Miller CL, et al. Atheroprotective roles of smooth muscle cell phenotypic modulation and the TCF21 disease gene as revealed by single-cell analysis. Nat Med. 2019;25(8):1280-9.
18. Uhlen M, Fagerberg L, Hallstrom BM, Lindskog C, Oksvold P, Mardinoglu A, et al. Proteomics. Tissue-based map of the human proteome. Science. 2015;347(6220):1260419.
19. Naylor AR, Rothwell PM, Bell PR. Overview of the principal results and secondary analyses from the European and North American randomised trials of endarterectomy for symptomatic carotid stenosis. Eur J Vasc Endovasc Surg. 2003;26(2):115-29.
20. Halliday A, Harrison M, Hayter E, Kong X, Mansfield A, Marro J, et al. 10-year stroke prevention after successful carotid endarterectomy for asymptomatic stenosis (ACST-1): a multicentre randomised trial. Lancet. 2010;376(9746):1074-84.

ACCEPTED MANUSCRIPT

Downloaded from https://academic.oup.com/cardiovascres/advance-article/doi/10.1093/cvr/cvaf210/8316259 by Turku University Language Centre user on 10 November 2025

21. Perisic L, Aldi S, Sun Y, Folkersen L, Razuvaev A, Roy J, et al. Gene expression signatures, pathways and networks in carotid atherosclerosis. J Intern Med. 2016;279(3):293-308.
22. Perisic Matic L, Rykaczewska U, Razuvaev A, Sabater-Lleal M, Lengquist M, Miller CL, et al. Phenotypic Modulation of Smooth Muscle Cells in Atherosclerosis Is Associated With Downregulation of LMOD1, SYNPO2, PDLIM7, PLN, and SYNM. Arterioscler Thromb Vasc Biol. 2016;36(9):1947-61.
23. Matic LP, Jesus Iglesias M, Vesterlund M, Lengquist M, Hong MG, Saieed S, et al. Novel Multiomics Profiling of Human Carotid Atherosclerotic Plaques and Plasma Reveals Biliverdin Reductase B as a Marker of Intraplaque Hemorrhage. JACC Basic Transl Sci. 2018;3(4):464-80.
24. Franzen O, Ermel R, Cohain A, Akers NK, Di Narzo A, Talukdar HA, et al. Cardiometabolic risk loci share downstream cis- and trans-gene regulation across tissues and diseases. Science. 2016;353(6301):827-30.
25. Koplev S, Seldin M, Sukhavasi K, Ermel R, Pang S, Zeng L, et al. A mechanistic framework for cardiometabolic and coronary artery diseases. Nat Cardiovasc Res. 2022;1(1):85-100.
26. Wik L, Nordberg N, Broberg J, Bjorkesten J, Assarsson E, Henriksson S, et al. Proximity Extension Assay in Combination with Next-Generation Sequencing for High-throughput Proteome-wide Analysis. Mol Cell Proteomics. 2021;20:100168.
27. Moisio O, Palani S, Virta J, Elo P, Liljenback H, Tolvanen T, et al. Radiosynthesis and preclinical evaluation of [(68)Ga]Ga-NOTA-folate for PET imaging of folate receptor beta-positive macrophages. Sci Rep. 2020;10(1):13593.
28. Palani S, Miner MWG, Virta J, Liljenback H, Eskola O, Ord T, et al. Exploiting Glutamine Consumption in Atherosclerotic Lesions by Positron Emission Tomography Tracer (2S,4R)-4-(18)F-Fluoroglutamine. Front Immunol. 2022;13:821423.
29. Miner MW, Liljenback H, Virta J, Merisaari J, Oikonen V, Westermarck J, et al. (2S, 4R)-4-[(18)F]Fluoroglutamine for In vivo PET Imaging of Glioma Xenografts in Mice: an Evaluation of Multiple Pharmacokinetic Models. Mol Imaging Biol. 2020;22(4):969-78.
30. Long JZ, Jacobson MS, Hung JC. Comparison of FASTlab 18F-FDG production using phosphate and citrate buffer cassettes. J Nucl Med Technol. 2013;41(1):32-4.
31. Silvola JMU, Li XG, Virta J, Marjamaki P, Liljenback H, Hytonen JP, et al. Aluminum fluoride-18 labeled folate enables in vivo detection of atherosclerotic plaque inflammation by positron emission tomography. Sci Rep. 2018;8(1):9720.
32. Silvola JM, Saraste A, Laitinen I, Savisto N, Laine VJ, Heinonen SE, et al. Effects of age, diet, and type 2 diabetes on the development and FDG uptake of atherosclerotic plaques. JACC Cardiovasc Imaging. 2011;4(12):1294-301.
33. Fernando S, Judith G-G, Jorge C, Rafael A, Antonio Z, Aida O, et al. Defective Slc7a7 transport reduces systemic arginine availability compromising erythropoiesis and iron homeostasis. bioRxiv. 2021:2021.08.15.456393.
34. Giroud-Gerbetant J, Sotillo F, Hernandez G, Ruano I, Sebastian D, Fort J, et al. Defective Slc7a7 transport reduces erythropoietin compromising erythropoiesis. Mol Med. 2025;31(1):29.
35. Merlin J, Ivanov S, Dumont A, Sergushichev A, Gall J, Stunault M, et al. Non-canonical glutamine transamination sustains efferocytosis by coupling redox buffering to oxidative phosphorylation. Nat Metab. 2021;3(10):1313-26.

ACCEPTED MANUSCRIPT

Downloaded from https://academic.oup.com/cardiovascres/advance-article/doi/10.1093/cvr/cvaf210/8316259 by Turku University Language Centre user on 10 November 2025

36. Ewels PA, Peltzer A, Fillinger S, Patel H, Alneberg J, Wilm A, et al. The nf-core framework for community-curated bioinformatics pipelines. Nat Biotechnol. 2020;38(3):276-8.
37. Dobin A, Davis CA, Schlesinger F, Drenkow J, Zaleski C, Jha S, et al. STAR: ultrafast universal RNA-seq aligner. Bioinformatics. 2013;29(1):15-21.
38. Cunningham F, Achuthan P, Akanni W, Allen J, Amode MR, Armean IM, et al. Ensembl 2019. Nucleic Acids Res. 2019;47(D1):D745-D51.
39. Robinson MD, McCarthy DJ, Smyth GK. edgeR: a Bioconductor package for differential expression analysis of digital gene expression data. Bioinformatics. 2010;26(1):139-40.
40. Love MI, Huber W, Anders S. Moderated estimation of fold change and dispersion for RNA-seq data with DESeq2. Genome Biol. 2014;15(12):550.
41. Korotkevich G, Sukhov V, Budin N, Shpak B, Artyomov MN, Sergushichev A. Fast gene set enrichment analysis. bioRxiv. 2021:060012.
42. Castanza AS, Recla JM, Eby D, Thorvaldsdottir H, Bult CJ, Mesirov JP. Extending support for mouse data in the Molecular Signatures Database (MSigDB). Nat Methods. 2023;20(11):1619-20.
43. Mass E, Nimmerjahn F, Kierdorf K, Schlitzer A. Tissue-specific macrophages: how they develop and choreograph tissue biology. Nat Rev Immunol. 2023;23(9):563-79.
44. Thul PJ, Akesson L, Wiking M, Mahdessian D, Geladaki A, Ait Blal H, et al. A subcellular map of the human proteome. Science. 2017;356(6340).
45. Cochain C, Vafadarnejad E, Arampatzi P, Pelisek J, Winkels H, Ley K, et al. Single-Cell RNA-Seq Reveals the Transcriptional Landscape and Heterogeneity of Aortic Macrophages in Murine Atherosclerosis. Circ Res. 2018;122(12):1661-74.
46. Smart CD, Fehrenbach DJ, Wassenaar JW, Agrawal V, Fortune NL, Dixon DD, et al. Immune profiling of murine cardiac leukocytes identifies Trem2 as a novel mediator of hypertensive heart failure. Cardiovasc Res. 2023.
47. Jaitin DA, Adlung L, Thaiss CA, Weiner A, Li B, Descamps H, et al. Lipid-Associated Macrophages Control Metabolic Homeostasis in a Trem2-Dependent Manner. Cell. 2019;178(3):686-98 e14.
48. Ramachandran P, Dobie R, Wilson-Kanamori JR, Dora EF, Henderson BEP, Luu NT, et al. Resolving the fibrotic niche of human liver cirrhosis at single-cell level. Nature. 2019;575(7783):512-8.
49. Perugorria MJ, Esparza-Baquer A, Oakley F, Labiano I, Korosec A, Jais A, et al. Non-parenchymal TREM-2 protects the liver from immune-mediated hepatocellular damage. Gut. 2019;68(3):533-46.
50. Xiong X, Kuang H, Ansari S, Liu T, Gong J, Wang S, et al. Landscape of Intercellular Crosstalk in Healthy and NASH Liver Revealed by Single-Cell Secretome Gene Analysis. Mol Cell. 2019;75(3):644-60 e5.
51. Reyfman PA, Walter JM, Joshi N, Anekalla KR, McQuattie-Pimentel AC, Chiu S, et al. Single-Cell Transcriptomic Analysis of Human Lung Provides Insights into the Pathobiology of Pulmonary Fibrosis. Am J Respir Crit Care Med. 2019;199(12):1517-36.
52. Hendrikx T, Porsch F, Kiss MG, Rajcic D, Papac-Milicevic N, Hoebinger C, et al. Soluble TREM2 levels reflect the recruitment and expansion of TREM2(+) macrophages that localize to fibrotic areas and limit NASH. J Hepatol. 2022;77(5):1373-85.
53. Wang X, He Q, Zhou C, Xu Y, Liu D, Fujiwara N, et al. Prolonged hypernutrition impairs TREM2-dependent efferocytosis to license chronic liver inflammation and NASH development. Immunity. 2023;56(1):58-77 e11.

ACCEPTED MANUSCRIPT

Downloaded from https://academic.oup.com/cardiovascres/advance-article/doi/10.1093/cvr/cvaf210/8316259 by Turku University Language Centre user on 10 November 2025

54. Cuciuc V, Tshori S, Grib L, Sella G, Tuvali O, Volodarsky I, et al. Circulating Soluble TREM2 and Cardiovascular Outcome in Cohort Study of Coronary Atherosclerosis Patients. Int J Mol Sci. 2022;23(21).
55. Piollet M, Porsch F, Rizzo G, Kapser F, Schulz DJJ, Kiss MG, et al. TREM2 protects from atherosclerosis by limiting necrotic core formation. Nat Cardiovasc Res. 2024;3(3):269-82.
56. Torrents D, Estevez R, Pineda M, Fernandez E, Lloberas J, Shi YB, et al. Identification and characterization of a membrane protein (y+L amino acid transporter-1) that associates with 4F2hc to encode the amino acid transport activity y+L. A candidate gene for lysinuric protein intolerance. J Biol Chem. 1998;273(49):32437-45.
57. Pfeiffer R, Rossier G, Spindler B, Meier C, Kuhn L, Verrey F. Amino acid transport of y+L-type by heterodimers of 4F2hc/CD98 and members of the glycoprotein-associated amino acid transporter family. EMBO J. 1999;18(1):49-57.
58. Palacin M, Borsani G, Sebastio G. The molecular bases of cystinuria and lysinuric protein intolerance. Curr Opin Genet Dev. 2001;11(3):328-35.
59. Bodoy S, Sotillo F, Espino-Guarch M, Sperandeo MP, Ormazabal A, Zorzano A, et al. Inducible Slc7a7 Knockout Mouse Model Recapitulates Lysinuric Protein Intolerance Disease. Int J Mol Sci. 2019;20(21).
60. Demy DL, Carrere M, Noche R, Tauzin M, Le Bris M, Baek C, et al. The cationic amino acid exporter Slc7a7 is induced and vital in zebrafish tissue macrophages with sustained efferocytic activity. J Cell Sci. 2020;133(20).
61. Rotoli BM, Barilli A, Visigalli R, Ingoglia F, Milioli M, Di Lascia M, et al. Downregulation of SLC7A7 Triggers an Inflammatory Phenotype in Human Macrophages and Airway Epithelial Cells. Front Immunol. 2018;9:508.
62. Eraslan G, Drokhlyansky E, Anand S, Fiskin E, Subramanian A, Slyper M, et al. Single-nucleus cross-tissue molecular reference maps toward understanding disease gene function. Science. 2022;376(6594):eabl4290.
63. George J. TREM2 as an evolving therapeutic target in Alzheimer's disease. Neural Regen Res. 2023;18(12):2680-1.
64. Molgora M, Esaulova E, Vermi W, Hou J, Chen Y, Luo J, et al. TREM2 Modulation Remodels the Tumor Myeloid Landscape Enhancing Anti-PD-1 Immunotherapy. Cell. 2020;182(4):886-900 e17.
65. Rodriguez-Vieitez E, Ashton NJ. Plasma sTREM2: a potential marker of cerebrovascular injury in neurodegenerative disorders. Brain. 2021;144(11):3283-5.
66. Eldjarn GH, Ferkingstad E, Lund SH, Helgason H, Magnusson OT, Gunnarsdottir K, et al. Large-scale plasma proteomics comparisons through genetics and disease associations. Nature. 2023;622(7982):348-58.
67. Riksen NP, Ait Oufella H. Macrophage TREM2 as a new player in atherosclerosis. Nat Cardiovasc Res. 2023;2(12):1117-9.
68. Patterson MT, Firulyova MM, Xu Y, Hillman H, Bishop C, Zhu A, et al. Trem2 promotes foamy macrophage lipid uptake and survival in atherosclerosis. Nat Cardiovasc Res. 2023;2(11):1015-31.
69. Patterson MT, Xu Y, Hillman H, Osinski V, Schrank PR, Kennedy AE, et al. Trem2 Agonist Reprograms Foamy Macrophages to Promote Atherosclerotic Plaque Stability. Arterioscler Thromb Vasc Biol. 2024.
70. Tawakol A, Fayad ZA, Mogg R, Alon A, Klimas MT, Dansky H, et al. Intensification of statin therapy results in a rapid reduction in atherosclerotic inflammation: results of a

ACCEPTED MANUSCRIPT

Downloaded from https://academic.oup.com/cardiovascres/advance-article/doi/10.1093/cvr/cvaf210/8316259 by Turku University Language Centre user on 10 November 2025

multicenter fluorodeoxyglucose-positron emission tomography/computed tomography feasibility study. J Am Coll Cardiol. 2013;62(10):909-17.
71. Rudd JH, Myers KS, Bansilal S, Machac J, Rafique A, Farkouh M, et al. (18)Fluorodeoxyglucose positron emission tomography imaging of atherosclerotic plaque inflammation is highly reproducible: implications for atherosclerosis therapy trials. J Am Coll Cardiol. 2007;50(9):892-6.
72. Bengel FM. Imaging of Post-Infarct Inflammation: Moving Forward Toward Clinical Application. Circ Cardiovasc Imaging. 2016;9(4):e004713.
73. Fox JJ, Strauss HW. One step closer to imaging vulnerable plaque in the coronary arteries. J Nucl Med. 2009;50(4):497-500.
74. Jha AK, Huang SC, Sergushichev A, Lampropoulou V, Ivanova Y, Loginicheva E, et al. Network integration of parallel metabolic and transcriptional data reveals metabolic modules that regulate macrophage polarization. Immunity. 2015;42(3):419-30.
75. Tavakoli S, Downs K, Short JD, Nguyen HN, Lai Y, Jerabek PA, et al. Characterization of Macrophage Polarization States Using Combined Measurement of 2-Deoxyglucose and Glutamine Accumulation: Implications for Imaging of Atherosclerosis. Arterioscler Thromb Vasc Biol. 2017;37(10):1840-8.
76. Barilli A, Rotoli BM, Visigalli R, Bussolati O, Gazzola GC, Gatti R, et al. Impaired phagocytosis in macrophages from patients affected by lysinuric protein intolerance. Mol Genet Metab. 2012;105(4):585-9.
77. Kurko J, Vaha-Makila M, Tringham M, Tanner L, Paavanen-Huhtala S, Saarinen M, et al. Dysfunction in macrophage toll-like receptor signaling caused by an inborn error of cationic amino acid transport. Mol Immunol. 2015;67(2 Pt B):416-25.

ACCEPTED MANUSCRIPT

Downloaded from https://academic.oup.com/cardiovascres/advance-article/doi/10.1093/cvr/cvaf210/8316259 by Turku University Language Centre user on 10 November 2025